

# Atmosphere-Ocean CO<sub>2</sub> Exchange Across the Last Deglaciation

## from the Boron Isotope Proxy

**Jun Shao<sup>1</sup>, Lowell D. Stott<sup>1</sup>, William R. Gray<sup>2, 3</sup>, Rosanna Greenop<sup>2</sup>, Ingo Pecher<sup>4</sup>, Helen L. Neil<sup>5</sup>, Richard B. Coffin<sup>6</sup>, and Bryan Davy<sup>7</sup>, James W.B. Rae<sup>2</sup>**

<sup>1</sup> Department of Earth Science, University of Southern California, Los Angeles, USA

<sup>2</sup> School of Earth and Environmental Sciences, University of St Andrews, St Andrews, UK

<sup>3</sup> Laboratoire des Sciences du Climat et de l'Environnement (LSCE/IPSL), Gif-sur-Yvette, France

<sup>4</sup> School of Environment, University of Auckland, Auckland, New Zealand

<sup>5</sup> Department of Marine Geology, the National Institute of Water and Atmospheric Research, New Zealand

<sup>6</sup> Department of Physical and Environmental Sciences, Texas A&M University-Corpus Christi, USA

<sup>7</sup> Department of Marine Geosciences, GNS Science, New Zealand

Corresponding author: Jun Shao ([junshao@usc.edu](mailto:junshao@usc.edu))

### Key Points:

- Boron-isotope based pH reconstructions indicate that the subtropical/subpolar Southwest

This is the author manuscript accepted for publication and has undergone full peer review but Pacific was a source of CO<sub>2</sub> during the last 19 ka. has not been through the copyediting, typesetting, pagination and proofreading process, which may lead to differences between this version and the Version of Record. Please cite this article as doi: [10.1029/2018PA003498](https://doi.org/10.1029/2018PA003498)

- Major CO<sub>2</sub> outgassing from the Southwest Pacific was associated with enhanced ventilation of intermediate waters between 16.5-14 kyrBP.
- A surface pH/pCO<sub>2</sub> composite derived from 12 planktic  $\delta^{11}\text{B}$  records shows widespread CO<sub>2</sub> release from the ocean during the last deglaciation.

## Abstract

Identifying processes within the Earth System that have modulated atmospheric pCO<sub>2</sub> during each glacial cycle of the late Pleistocene stands as one of the grand challenges in climate science. The growing array of surface ocean pH estimates from the boron isotope proxy across the last glacial termination may reveal regions of the ocean that influenced the timing and magnitude of pCO<sub>2</sub> rise. Here we present two new boron isotope records from the subtropical-subpolar transition zone of the Southwest Pacific that span the last 20 kyr, as well as new radiocarbon data from the same cores. The new data suggest this region was a source of carbon to the atmosphere rather than a moderate sink as it is today. Significantly higher outgassing is observed between ~16.5-14 kyrBP, associated with increasing  $\delta^{13}\text{C}$  and  $[\text{CO}_3]^{2-}$  at depth, suggesting loss of carbon from the intermediate ocean to the atmosphere. We use these new boron isotope records together with existing records to build a composite pH/pCO<sub>2</sub> curve for the surface oceans. pH disequilibrium/CO<sub>2</sub> outgassing was widespread throughout the last deglaciation, likely explained by upwelling of CO<sub>2</sub> from the deep/intermediate ocean. During the Holocene, a smaller outgassing peak is observed at a time of relatively stable atmospheric CO<sub>2</sub>, which may be explained by regrowth of the terrestrial biosphere countering ocean CO<sub>2</sub> release. Our stack is likely biased toward upwelling/CO<sub>2</sub> source regions. Nevertheless, the composite pCO<sub>2</sub> curve

provides robust evidence that various parts of the ocean were releasing CO<sub>2</sub> to the atmosphere over the last 25 kyr.

## 1. Introduction

Growth and retreat of ice sheets in the late Pleistocene was accompanied by variations in atmospheric pCO<sub>2</sub> from ~180 ppm during the glacial maxima to 280 ppm during peak preindustrial interglacials (Petit et al., 1999). Most explanations for this CO<sub>2</sub> change have focused on a more efficient polar-ocean biological pump, driven by a combination of increased stratification (Basak et al., 2018; Ferrari et al., 2014; Francois et al., 1997) and stronger iron fertilization in the Southern Ocean (Martinez-Garcia et al., 2014). Reduced hydrothermal flux of CO<sub>2</sub> has also recently been suggested to play a role (Lund et al., 2016; Stott & Timmermann, 2011). However, the relative importance and timing of the mechanisms that contributed to glacial CO<sub>2</sub> change is yet to be fully resolved.

To improve constraints on the role of ocean-atmosphere CO<sub>2</sub> exchange between the ocean and the atmosphere in glacial-interglacial changes in atmospheric pCO<sub>2</sub>, several recent studies have examined when and where CO<sub>2</sub> was entering and leaving the ocean using sea surface carbonate chemistry reconstructions. Changes in surface CO<sub>2</sub> chemistry may be driven by changes in upwelling or stratification, and changes in the biological soft tissue and CaCO<sub>3</sub> pumps. In turn these influence CO<sub>2</sub> gas exchange, which is determined by the CO<sub>2</sub> partial pressure gradient between the surface ocean and the atmosphere ( $\Delta p\text{CO}_2$ ) and the gas exchange coefficient, which is affected by wind speed. Tracking past air-sea CO<sub>2</sub> exchange may help test hypotheses that have been put forward to explain glacial/interglacial atmospheric pCO<sub>2</sub> variability.

Author Manuscript

The boron isotope composition ( $\delta^{11}\text{B}$ ) of foraminifera is a proxy for oceanic pH (Foster & Rae, 2016; Hemming & Hanson, 1992; Hönisch & Hemming, 2005). This proxy is based on the pH-dependency of boron speciation in seawater between boric acid ( $\text{B}(\text{OH})_3$ ) and borate ion ( $\text{B}(\text{OH})_4^-$ ) (Dickson, 1990). At low pH ( $< \sim 8.6$ ), seawater boron primarily exists in the form of boric acid, whereas at high pH ( $> \sim 8.6$ ), seawater boron is dominantly present in the form of borate. Because there is a constant equilibrium fractionation of 27.2‰ associated with this speciation (Klochko et al., 2006), the boron isotopic composition of each species is also pH dependent. A positive correlation between the boron isotope composition of planktic foraminifera and pH has been established through culturing experiments (Henahan et al., 2013; Sanyal et al., 1996, 2001). However, the  $\delta^{11}\text{B}$  in calcite from various foraminiferal species deviates from that of the borate in seawater to varying degrees. This may arise from biological processes, including respiration and photosynthesis that are collectively referred to as “vital effects” (Hönisch et al., 2003; Rae, 2018; Zeebe et al., 2003). As a result, species-specific calibrations have been developed from culturing experiments, sediment core-tops, sediment traps and plankton tows (Henahan et al., 2013, 2016; Sanyal et al., 1996).

By taking advantage of the calibrated boron-pH proxy, a number of studies have investigated the history of ocean-atmosphere  $\text{CO}_2$  exchange across the last deglaciation from sites in the tropical Pacific (Martínez-Botí et al., 2015; Palmer & Pearson, 2003), the North Pacific (Gray et al., 2018a), the North Indian Ocean (Naik et al., 2015; Palmer et al., 2010), the tropical Atlantic (Foster, 2008; Foster & Sexton, 2014; Henahan et al. 2013), the North Atlantic (Ezat et al., 2017; Yu et al., 2013) and the South Atlantic (Martínez-Botí et al., 2015) (Figure 1a). Collectively, the available records reveal millennial-scale  $\delta^{11}\text{B}$  variations that reflect substantial changes in air-sea  $\Delta p\text{CO}_2$  over the deglaciation (Figure 2). These variations have been

interpreted to reflect local or regional changes in upwelling intensity, the  $\text{CO}_2$  content of subsurface waters, and the efficiency of the biological pump. While each of these proposed mechanisms can be used to explain the individual  $\delta^{11}\text{B}$  records, the collective influence of these changes on air-sea  $\Delta\text{pCO}_2$  has not been evaluated. Here, we consider the implication of the combined reconstructed anomalies on the evolution of atmospheric  $\text{pCO}_2$ .

As the number of boron isotope records has expanded to various parts of the ocean, it may now be possible to evaluate how the records reflect global as well as local influences. However, the subtropical and subpolar South Pacific remain poorly constrained (Figure 1a). Hence, a global picture of the air-sea exchange of  $\text{CO}_2$  is far from complete without additional reconstructions from these areas. To address this, we present two new boron isotope reconstructions from cores recovered from Chatham Rise in the subtropical-subpolar transition zone of the SW Pacific. Although located in a moderate  $\text{CO}_2$  sink region today, this site may also be influenced by changes in ventilation and biological pump efficiency in the Southern Ocean (Allen et al., 2015; McCave et al., 2008; Studer et al., 2015), migration of the subtropical front (Bostock et al., 2015), and/or localized inputs of radiocarbon-dead carbon (Ronge et al., 2016) on glacial-interglacial timescales. We also generate new benthic-planktic radiocarbon data to trace how reconstructed changes in  $\text{CO}_2$  outgassing relate to changes in ventilation at depth. We combine our new boron isotope records with available records to build an initial composite sea surface pH reconstruction that spans the last 25 kyr and use this composite to assess whether the available data provide a realistic representation of global surface ocean surface  $\text{CO}_2$  exchange. Our null hypothesis is that a composite pH/ $\text{pCO}_2$  record that includes both source and sink regions constitutes a first-order representation of the equilibrium exchange of  $\text{CO}_2$  between the surface ocean and atmosphere over the last 25 kyr. The null hypothesis predicts: First, during

times of relatively stable atmospheric CO<sub>2</sub>, the composite ocean pCO<sub>2</sub> stack should be roughly in equilibrium with the atmosphere; second, during intervals when the oceans released CO<sub>2</sub> to the atmosphere, the composite pCO<sub>2</sub> should be higher than the contemporary atmospheric pCO<sub>2</sub>, with larger offsets occurring when atmospheric pCO<sub>2</sub> rose rapidly. Alternatively, the available records may be biased because of their locations, such that the regional ocean/atmosphere dynamics or extra carbon input from a local source overshadow the history of equilibrium exchange between the ocean and atmosphere. We test the null hypothesis in both the pH and the pCO<sub>2</sub> space. The boron isotope pH composite is evaluated against an independent estimation of the global mean equilibrium sea surface pH (GMSSpH), obtained by forcing the Earth System model cGENIE (Ridgwell et al., 2007; Cao et al., 2009) with the ice core record of atmospheric pCO<sub>2</sub> over the last 25 kyr (Bereiter et al., 2015; Monnin et al., 2001). In the model simulation, atmospheric pCO<sub>2</sub> data from ice cores are treated as a constraint instead of a problem to solve. We also compare the boron isotope-derived pCO<sub>2</sub> composite directly with the atmospheric pCO<sub>2</sub> record.

## **2. Methods:**

### **2.1 Oceanographic Settings for Cores PC75-2 and PC83-1**

In the SW Pacific today, the subtropical gyre between 20°S to 45°S is a carbon sink, while the surface waters south of the subtropical front (STF) between 45°S to 55°S are in near equilibrium with the atmosphere (Figure 1a). Cores PC75-2 (177°8.97' E, 44°14, 39' S; 967m water depth) and PC83-1 (177°2,49' E, 44°18,38' S; 1010m water depth) were retrieved by the RV *Sonne* from the southern flank of the Chatham Rise east of New Zealand. The core locations are close to the modern position of the Subtropical Front (STF), which separates cold, less salty

sub-Antarctic waters from warm, more saline subtropical waters (Coffin et al., 2013), and are bathed by Antarctic Intermediate Water (AAIW). Our core sites are located at the south edge of the subtropical CO<sub>2</sub> sink, with an annual mean modern  $\Delta p\text{CO}_2 = \sim -20\text{ppm}$  and a modest seasonal cycle of  $\sim 30\text{ ppm}$  (Figure 1b, Figure S1). Direct comparison between our paleo-reconstruction and modern  $\Delta p\text{CO}_2$  at the core site might be complicated by the following three factors (Figure S1): 1) our site is potentially sensitive to front shifts during the last deglaciation: everything else being equal, a northward shift of the STF during the Last Glacial Maximum (LGM) and early deglaciation (Bostock et al., 2015) would turn our core site into a weaker sink or even a minor source; 2) a sediment trap study suggests that flux of *Globigerina bulloides* is much higher near our site between September to February, when the CO<sub>2</sub> sink is weaker than rest of the year (Jonkers & Kučera, 2015); 3) strictly speaking, modern  $\Delta p\text{CO}_2$  may not be under a steady state (e.g. Holocene) due to anthropogenic CO<sub>2</sub> emissions.

## **2.2 Age Model for PC75-2 and PC83-1**

### **2.2.1 Radiocarbon Measurements:**

For reconstruction of radiocarbon activities, mixed planktic and benthic foraminifera from PC75-1; *Globorotalia inflata* (*G. inflata*), *G. bulloides* and mixed benthic foraminifera from PC75-2; *G. inflata* from PC83-1 were picked (Table S1). For PC75-1, radiocarbon was measured at the Rafter Radiocarbon Lab at the GNS Science National Isotope Centre. For PC75-2 and PC83-1, <sup>14</sup>C dating was carried out at the Keck Carbon Cycle Accelerator Mass Spectrometry Laboratory at University of California, Irvine. Samples were leached in 10% dilute HCL immediately prior to hydrolysis.

### **2.2.2 Stable Isotope Measurements:**

Approximately 20-30 *G. inflata* were picked from PC75-2 and PC83-1 at each interval for  $\delta^{18}\text{O}$  and  $\delta^{13}\text{C}$  measurements. These were analyzed on a dual inlet VG Micromass Isoprime stable isotope ratio mass spectrometer equipped with an autocarbonate system at University of Southern California. The precision of in-house calcite standards run in conjunction with the foraminiferal samples averaged  $\sim 0.15\text{‰}$  for  $\delta^{18}\text{O}$  and  $\sim 0.06\text{‰}$  for  $\delta^{13}\text{C}$  (2SD), over the course of the present study.

PC75-1 *G. inflata* and *Cibicides*  $\delta^{18}\text{O}$  and  $\delta^{13}\text{C}$  were analyzed by a Finnigan MAT 252 mass spectrometer at National Institute of Water and Atmospheric Research's (NIWA) stable isotope lab. Concurrently-run carbonate standards (NBS-19) had an internal precision of 0.08‰ for  $\delta^{18}\text{O}$  and  $\sim 0.04\text{‰}$  for  $\delta^{13}\text{C}$  (2SD).

#### **Age model:**

To develop an age model for the PC75 core location, we combined 6 new AMS  $^{14}\text{C}$  dates measured on calcite tests of the planktic foraminiferal species *G. inflata* and *G. bulloides* from PC75-2 and 4 AMS  $^{14}\text{C}$  dates from mixed planktic foraminifera from the co-located core PC75-1 core (Table S1). These two cores were taken from the same location but for different purposes. There was not enough material left from the PC75-1 core for both boron isotope analysis and radiometric dating. Therefore, samples from PC75-2 were used. The two cores have almost identical stratigraphies (Figure S2, Table S2). Each planktic  $^{14}\text{C}$  age was converted to calendar years using the BChron Bayesian chronology package (Haslett & Parnell, 2008), with the marine calibration dataset – MARINE13 (Reimer et al., 2013). This dating technique requires some knowledge of surface reservoir ages. Surface reservoir ages of the SW Pacific Ocean at various times during the last 25 kyr have been obtained in previous studies by pairing radiocarbon measurements of marine carbonates deposited above and/or below volcanic tephra layers (Sikes



et al., 2000; Sikes & Guilderson, 2016; Skinner et al., 2015). The chronologic ages of the tephra have been constrained by radiocarbon dating terrestrial organic material from land-based deposits that contain the same tephra. By applying the up-to-date global calibration curve IntCal 13 (Reimer et al., 2013), Sikes and Guilderson (2016) concluded that surface reservoir ages during the late deglaciation and early Holocene were not significantly different from modern values. We therefore applied a reservoir age of  $400 \pm 100$  yrs for each radiocarbon date from the core top to 110 cm, the oldest late deglacial interval where radiocarbon dates are available. We identified the 'Kawakawa' tephra layer between 343-349cm in core PC75-1. The tephra has a calendar age of  $25,650 \pm 40$  yr BP (Lowe et al., 2013; Sikes & Guilderson, 2016), which corresponds to an atmospheric  $^{14}\text{C}$  age of 21299 yr according to the Intcal13 calibration. Right below this tephra layer, the planktic  $^{14}\text{C}$  age at 350cm is 22904 yr, which gives an estimate of late glacial reservoir age  $\sim 1600$  yrs. In a previous study using the same paired tephra-foraminifera dating technique on a core off New Zealand and located just north of the subtropical/subpolar boundary, the estimated surface reservoir ages were  $\sim 1000$  yrs during the late glacial and  $\sim 1250$  yrs during the early deglaciation (Skinner et al., 2015). Taking these results together, we applied reservoir ages of  $\sim 1300 \pm 200$  yrs to our late glacial and early deglacial samples. To provide further age constraints, we utilized an additional chronologic datum: the beginning of the deglacial transition in the benthic  $\delta^{18}\text{O}$  isotope stratigraphy of PC75-1, which occurs at 165cm (Table S3). The regional deglacial transition at intermediate water depths of the SW Pacific has been dated at  $\sim 16200$ - $16900$  yrBP (Stern & Lisiecki, 2014). We therefore, assigned an age of  $16500 \pm 150$  yrBP to the 165cm horizon. The calibrated ages from radiocarbon measurements and the two extra age control points (tephra layer and  $\delta^{18}\text{O}$  transition) were used as tie points to develop the age model for PC75-2.

The age model for PC83-1 is based on 3 AMS  $^{14}\text{C}$  dates, and the reservoir ages are same as those applied to the PC75 record since the two sites are very close to each other. An additional age constraint comes from aligning the stable isotope stratigraphy of PC75-2 and PC83-1 (Figure S3, Table S2). For the intervals where there are no planktic  $^{14}\text{C}$  dates or other age control, a linear interpolation has been used to estimate ages. We note that ages in PC83 are relatively uncertain, given the low resolution of our age control points, and this may be a source of uncertainty when comparing deglacial  $\delta^{11}\text{B}$  data from these different sites. For a summary of applied reservoir ages and Bchron calibrated ages, see Table S4.

### 2.3 Trace Element and $\delta^{11}\text{B}$ Analyses

Approximately 100-200 tests of *G. bulloides* were picked from the 250-350  $\mu\text{m}$  size fraction for trace element and  $\delta^{11}\text{B}$  analyses (Table S5). Sample preparations were carried out in a low-boron clean lab at the University of St Andrews. Samples were cleaned based on the “Mg-cleaning” oxidation procedure (Barker et al., 2003; Rae et al., 2011). An aliquot (~3% of the total sample) was taken for trace element analyses, which were performed on an Agilent 7500 ICP-MS at the University of St Andrews using matrix-matched standards. Long-term reproducibility of Mg/Ca and B/Ca using this method is 1.2% and 2.3% (2 SD), respectively. Boron was separated from the sample matrix using Amberlite IRA-743 boron specific anion exchange resin, following the protocols of Foster (2008) and Foster et al., (2013).  $\Delta^{11}\text{B}$  was measured on a Thermo Scientific Neptune MC-ICP-MS at the University of St Andrews, based on protocols described in Foster (2008), Rae et al., (2011), and Rae et al., (2018), but with the addition of high ohmage ( $10^{13} \Omega$ ) resistors and triplicate sample analyses. Samples were corrected for total procedural blank, which averaged 33 pg in this session. Rae et al. (2011) previously reported uncertainties of  $\pm 0.23 \text{ ‰}$  (2 SD) for samples of ~20 ng, increasing at smaller

sample sizes. This has been improved given the developments in analyses described above. For example a boric acid standard (ERM-AE121; Vogl & Rosner, 2012) run during these sessions at the same concentration and under the same conditions as these samples (15 ppb) gave  $\delta^{11}\text{B} = 19.59 \pm 0.14 \text{ ‰}$  (2SD,  $n = 8$ ); and replicate purifications and measurements of a dissolved carbonate standard with a composition mimicking planktic foraminifera, and run under these conditions at a concentration of 7 ppb, gave 2SD of 0.20 ‰ ( $n = 12$ ). However as full description and quantification of this updated method is beyond the scope of the current study, and as the signals found here are large compared to analytical uncertainty, we assign conservative analytical uncertainties following the relationships in Rae et al. (2011). Prior to  $\delta^{11}\text{B}$  analysis, samples were screened for potential contamination by checking various elemental ratios (B/Ca, Mg/Ca and Al/Ca). A few samples had elevated Al/Ca ratios (up to about 200-300  $\mu\text{mol/mol}$ ) but showed no correlation with either  $\delta^{11}\text{B}$  or Mg/Ca (Figure S4).

### 2.3 Salinity estimate:

To estimate sea surface salinity (SSS) changes some authors have previously combined Mg/Ca and  $\delta^{18}\text{O}$  of planktic foraminifera under the assumption that the amount of  $\delta^{18}\text{O}$  change that cannot be accounted for by the Mg/Ca-derived temperature change must reflect a change in the oxygen isotopic composition of sea water, which is affected by salinity (Ezat et al., 2017; Naik et al., 2015). However, this approach assumes a constant relationship between salinity and the  $\delta^{18}\text{O}$  of seawater; this assumption is unlikely to hold over G-IG timescales and can therefore result in large biases within the resulting salinity reconstruction. Given modelled regional changes in salinity are relatively small throughout most of the ocean during the LGM (Gray and Evans, 2019), we followed the approach outlined in Gray and Evans (2019) and calculate salinity as the modern salinity at our site plus the modelled mean surface ocean glacial salinity increase

(0.7 PSU) scaled to global sea level (using the curve of Spratt & Lisiecki 2016), with an uncertainty of  $\pm 1$  PSU ( $2\sigma$ ). For any individual core, the two methods of salinity estimate would only introduce minor differences in reconstructed pH/pCO<sub>2</sub> values (Hönisch & Hemming, 2005). When developing a composite, one advantage of our approach is that removal of the long-term sea level influence on SSS, residual local SSS variations between sites are likely uncorrelated and would not systematically impact reconstruct pH/pCO<sub>2</sub> between sites.

## 2.4 Paired SST/pH and pCO<sub>2</sub> estimate

pH influences the Mg/Ca of planktic foraminifera (Evans et al., 2016; Gray et al., 2018b; Kısakürek et al., 2008; Lea et al., 1999; Russell et al., 2004). Temperature estimates from Mg/Ca are in turn required to calculate the boric acid and carbonate system dissociation constants (e.g. Dickson, 1990), and thus pH and pCO<sub>2</sub>. Here, we apply a recently developed algorithm (Gray & Evans, 2019) that iteratively solves Mg/Ca and  $\delta^{11}\text{B}_{\text{borate}}$  for SST and pH, overcoming the covariance induced between pH and temperature due to the thermal control on the carbonate system and boric acid dissociation constants. Mg/Ca based SSTs estimated from this method are more consistent with alkenone based SST estimates over deglaciation (Gray & Evans, 2019), thus carbonate system and boric acid dissociation constant estimates (and therefore pH and pCO<sub>2</sub>) will also be more accurate. We use the *G. bulloides* Mg/Ca calibration given in Gray & Evans (2019), based on foraminifera grown in laboratory culture. Partial dissolution of planktic foraminiferal tests lowers Mg/Ca (Regenberg et al., 2014); we note, it does not affect  $\delta^{11}\text{B}$  (Edgar et al., 2015). Here, we calculate temperature downcore as the temperature anomaly from the mean Holocene (0-10 ka) temperature, assuming the mean annual climatological temperature for the Holocene; this approach assumes the effects of dissolution have remained ~constant through time.

The ability to derive estimates of pH from the  $\delta^{11}\text{B}$  of foraminiferal calcite stems from the fact that the borate ion is the dominant species incorporated into  $\text{CaCO}_3$  (Hemming & Hanson, 1992; Rae, 2018; Rae et al., 2011). The methodology of transforming the boron isotopic composition of foraminifera to an estimate of ocean pH has recently been reviewed by Foster and Rae (2016) and Rae (2018). In the present study,  $\delta^{11}\text{B}_{\text{borate}}$  is derived using the species-specific calibration for *G. bulloides* determined by a Monte Carlo/wild bootstrap approach (Henehan et al., 2016) where,  $\delta^{11}\text{B}_{\text{borate}} = (\delta^{11}\text{B}_{\text{CaCO}_3} + 3.58 \pm 11.77)/1.09 \pm 0.65$  (Raitzsch et al., 2018), which has a wider range of uncertainty than used by Martínez-Botí et al. (2015). The  $\delta^{11}\text{B}_{\text{borate}}$  value is then used to estimate pH using the accurate formula from Rae (2018).

The estimate of local seawater  $\text{pCO}_2$  from the pH value requires an assumption about a second parameter of the carbonate system, typically the local sea surface alkalinity (ALK), which is poorly constrained for the glacial and deglacial ocean. To estimate sea surface ALK some authors have applied a modern local SSS-ALK regression relationship, using estimates of paleo-SSS (Ezat et al., 2017; Martínez-Botí et al., 2015; Naik et al., 2015). This assumes that most of the variability in ALK and SSS are dominated by evaporation and precipitation and/or sea level changes. However, SSS and ALK could be decoupled due to changes in riverine input of ALK, nutrient uptake, and remineralization, and production and export of  $\text{CaCO}_3$  (Fry et al., 2015). Thus, applying the modern local SSS-ALK regression could introduce significant bias. In a previous study, Martínez-Botí et al., (2015) randomly varied ALK between the modern value at the site today  $+125 \mu\text{mol/kg}$  (Hain et al., 2010; Toggweiler, 1999) to  $-25 \mu\text{mol/kg}$  with a flat distribution given that knowledge of the secular evolution of ALK during the last deglaciation is currently lacking. However it is possible that, even with higher whole ocean alkalinity, sea surface ALK was not much different from modern values due to stronger ocean stratification and

the deep remineralization profile of  $\text{CaCO}_3$ . We therefore randomly vary ALK between ‘modern plus 75  $\mu\text{mol/kg}$ ’ to ‘modern minus 75  $\mu\text{mol/kg}$ ’ in each  $\text{pCO}_2$  calculation. Note that this uncertainty range is large, encompassing much of the variability of the modern ocean. Also resulting uncertainty on  $\text{pCO}_2$  remains dominated by the uncertainty on  $\delta^{11}\text{B}$ -derived pH, given the close coupling of pH and  $\text{CO}_2$  within the carbonate system (Rae 2018).

pH and seawater  $\text{pCO}_2$  for each sample horizon is calculated using the ‘seacarb’ package in R (<https://CRAN.R-project.org/package=seacarb>). To fully propagate the uncertainties associated with pH/ $\text{pCO}_2$  estimations, we ran 10,000 Monte Carlo simulations that included the following uncertainties (2SE): analytical uncertainty on  $\delta^{11}\text{B}_{\text{CaCO}_3}$ , salinity  $\pm 1$  PSU, Mg/Ca calibration uncertainty,  $\delta^{11}\text{B}_{\text{CaCO}_3}$ - $\delta^{11}\text{B}_{\text{borate}}$  calibration uncertainty.

## 2.5 Composite pH and Seawater $\text{pCO}_2$

We compiled 10 previously published and 2 new (this study) boron-based pH/seawater  $\text{pCO}_2$  reconstructions with millennial-scale resolution spanning the last 25 kyr. RAPiD-15-4P (Yu et al., 2013) is not included in the composite because both Holocene and LGM intervals are missing in this record (Figure 2). We recalculated pH and seawater  $\text{pCO}_2$  from each published boron isotope value with a self-consistent framework. This includes modifying published estimations of 1) SST; 2) SSS; and 3) the carbonate  $\delta^{11}\text{B}$  to  $\delta^{11}\text{B}_{\text{borate}}$  in seawater. The SSS and SST changes for each record are recalculated in the manner described in section 2.3 and 2.4, with species-specific Mg/Ca calibrations from Gray & Evans (2019). Calculating seawater  $\delta^{11}\text{B}_{\text{borate}}$  from the foraminiferal  $\delta^{11}\text{B}$  under a self-consistent framework is not a trivial task since the records were generated using different machines and/or techniques. The pioneering work on the species-specific  $\delta^{11}\text{B}$  calibration was conducted on negative Thermal Ionization Mass

Spectrometry (N-TIMS) (Sanyal et al., 1996, 2001). More recently, Multicollector-Inductively Coupled Plasma Mass Spectrometry (MC-ICPMS) has been used for boron isotope analyses of marine carbonates (Foster, 2008). However, measured  $\delta^{11}\text{B}$  from the same planktic species (see figure 2a for example) or even homogenized calcite samples (Farmer et al., 2016) are lower on ICPMS than NTIMS by up to several per mil in some cases. Currently, this technique offset is not easily explained (see Farmer et al., 2016), but may be possible to correct. Logically, the same slopes ‘m’ (i.e. pH sensitivities) should be applied to all records using the same species, no matter which technique was used to generate the boron isotope data. Indeed, studies suggest that the calibration slope may be transferable between different measurement techniques (Farmer et al., 2016; Foster et al., 2013). Therefore, the correction involves applying a constant offset to the established species-specific calibrations.

The slope (‘m’) of the foraminiferal  $\delta^{11}\text{B}_{\text{CaCO}_3}$  vs  $\delta^{11}\text{B}_{\text{borate}}$  in seawater has been determined through culturing, core-top and sediment trap data sampling using both techniques (Henahan et al., 2013; Martínez-Botí et al., 2015; Sanyal et al., 2001). Our strategy is to apply the latest species-specific calibration curves that include newer data and more robust statistical techniques. The calibration curve for *Globigerinoides ruber* and *G. bulloides* comes from Raitzsch et al., (2018). For *Trilobatus sacculifer*, the intercept presented in Raitzsch et al., (2018) is offset from that of Henahan et al., (2016) by  $\sim 0.8\text{‰}$  with essentially the same slope. This is because one culture data point from Sanyal et al., (2001) was misplaced (i.e. one  $\delta^{11}\text{B}_{\text{CaCO}_3}$  data should be  $18.49\text{‰}$  not  $18.9\text{‰}$ ) by Raitzsch et al., (2018) and more core-top data were included in that study. To let our recalculated pH/pCO<sub>2</sub> be close to original published values, we chose the calibration curve from Henahan et al., 2016 for *T. sacculifer*. The calibration used for *Neogloboquadrina pachyderma* (*N. pachyderma*) is  $\delta^{11}\text{B}_{\text{borate}} = \delta^{11}\text{B}_{\text{CaCO}_3} + 3.38 \pm 0.72\text{‰}$  (first calibrated by Yu et

al., 2013, later confirmed by Gray et al., 2018a over a wider range of pH). For the *N. pachyderma* JM11 record generated by NTIMS (Ezat et al., 2017), we used the original intercept of 2.053‰ (Ezat et al., 2017, NTIMS) instead of 3.38‰ (Gray et al., 2018a, MC-ICP-MS) to account for technique/machine offsets. Applying the *T. sacculifer* calibration curve to the Holocene  $\delta^{11}\text{B}$  of NIOP464 (Palmer et al., 2010, NTIMS) and EDRC92 (Palmer & Pearson, 2003, NTIMS) resulted in very different pH from the original publication, due to technique/machine offsets. Thus, we modified the intercept such that the average Holocene pH from each record equals the pre-industrial sea surface pH at the core site that is derived from the GLODAP V2 2016b dataset. Table 1 summarizes the regression applied for each individual record. Where possible we use reported analytical uncertainty of  $\delta^{11}\text{B}$ ; Palmer & Pearson (2003) and Palmer et al., (2010) did not report analytical uncertainties, so we use  $\pm 0.3\text{‰}$  (2 SE). The procedure described in section 2.4 is then applied to calculate pH and  $\text{pCO}_2$  for each data point. We term the results as ‘ $\text{pH}_{\text{boron}}$ ’ and ‘ $\text{pCO}_{2\text{boron}}$ ’. When we developed the pH and  $\text{pCO}_2$  composite, we treated each ‘ $\text{pH}_{\text{boron}}$ ’ and ‘ $\text{pCO}_{2\text{boron}}$ ’ data point as a sample of the global mean sea surface pH and  $\text{pCO}_2$ . However,  $\delta^{11}\text{B}$ -based pH reconstructions may carry a bias relative to the true mean pH at a specific sample site (‘reconstruction bias’) and true mean pH at each site carries a bias relative to mean global pH (‘location bias’). For each individual record, the ‘reconstruction bias’ is estimated by the difference between the average  $\text{pH}_{\text{boron}}$  over the Holocene ( $\text{pH}_{\text{boron\_Holocene}}$ ) and pre-industrial pH at that site ( $\text{pH}_{\text{site\_preind}}$ ) from the GLODAP V2 2016b product (Lauvset et al., 2016); the ‘location bias’ is estimated by the difference between  $\text{pH}_{\text{site\_preind}}$  and the global pre-industrial pH from the same GLODAP product (‘ $\text{pH}_{\text{global\_preind}}$ ’). The expression for the final pH data is then:  $\text{pH}_{\text{final}} = \text{pH}_{\text{boron}} - (\text{pH}_{\text{boron\_Holocene}} - \text{pH}_{\text{site\_preind}}) - (\text{pH}_{\text{site\_preind}} - \text{pH}_{\text{global\_preind}}) = \text{pH}_{\text{boron}} - \text{pH}_{\text{boron\_Holocene}} + \text{pH}_{\text{global\_preind}}$ . The uncertainty of ‘ $\text{pH}_{\text{boron\_Holocene}}$ ’ and ‘ $\text{pH}_{\text{global\_preind}}$ ’ are then



propagated into using 10,000 Monte Carlo simulations, along with a  $\pm 700$ -year age error (2 SE) for each sample age. The same procedure is applied to  $p\text{CO}_2$ :  $p\text{CO}_{2\text{final}} = p\text{CO}_{2\text{boron}} - (p\text{CO}_{2\text{boron\_Holocene}} - p\text{CO}_{2\text{site\_preind}}) - (p\text{CO}_{2\text{site\_preind}} - p\text{CO}_{2\text{global\_preind}}) = p\text{CO}_{2\text{boron}} - p\text{CO}_{2\text{boron\_Holocene}} + p\text{CO}_{2\text{global\_preind}}$ . The final pH/ $p\text{CO}_2$  data from each of the cores were then binned into 1000-year intervals, and the average pH/ $p\text{CO}_2$  for each bin was calculated.

We note here that when we discuss the deglacial history of sea surface pH/ $p\text{CO}_2$  in the SW Pacific in section 3.1 and 4.1, we report and refer to the uncorrected  $p\text{H}_{\text{boron}}$  and  $p\text{CO}_{2\text{boron}}$  values from PC75-2 and PC83-1. On the other hand, when we discuss the global composite pH/ $p\text{CO}_2$  in section 3.2 and 4.2, we refer to the corrected  $p\text{H}_{\text{final}}$  and  $p\text{CO}_{2\text{final}}$  from 12 records.

## 2.6 Modeling the GMSSpH with cGENIE Earth System Model

The Earth System model cGENIE was used to develop a simulated GMSSpH over the last 25 kyr to compare against the composite pH curve. The cGENIE model includes a 3-D dynamical ocean model coupled to the 2-D energy-moisture balance atmospheric model (Edwards & Marsh, 2005). The ocean model is based on a 36x36 horizontal grid with 16 vertical layers. cGENIE has a dynamic and thermodynamic component of sea ice. The model also incorporates a marine biogeochemical cycling of carbon and other tracers (Ridgwell et al., 2007). All simulations in the present study used a pre-industrial configuration (Cao et al., 2009) and were spun up as a closed system for 20 kyr.

To estimate the GMSSpH over the last 25 kyr, an ‘LGM’ like sea surface carbonate chemistry state is a necessary initial condition for the model. Since an investigation of carbonate system feedbacks is not the purpose of this study, interactive sediments (i.e. open-system configurations) are not used in the following simulation. We achieved a peak glacial atmospheric

pCO<sub>2</sub> value through an inverse approach with three end-member scenarios. Specifically, in scenario 1 ALK is added to the surface ocean; in scenario 2 ALK and DIC are added to the surface ocean in a 2:1 ratio (i.e. CaCO<sub>3</sub> addition); in scenario 3 DIC is subtracted from the surface ocean. We performed the inversion under a modern ocean circulation for 10,000 years. The resulting ‘LGM’ atmospheric pCO<sub>2</sub> and sea water chemistry responses at the end of the inversion are summarized in Table 2. Since the GMSSpH is strongly coupled to the atmospheric pCO<sub>2</sub>, we would get essentially the same answer even if we apply an ‘LGM’ like circulation scenario (not shown). Then, to estimate the GMSSpH over the last 25 kyr, a transient carbon flux was added or taken out of the atmosphere so that the atmospheric pCO<sub>2</sub> follows the ice core record.

### 3 Results

#### 3.1 Two New Boron Isotope-Based pH Reconstructions from the SW Pacific

The new  $\delta^{11}\text{B}$  record from subtropical South Pacific core PC75-2 is shown in Figure 3a. This core documents ~1.5‰ lower values during the early deglacial relative to the glacial and late deglacial samples and shows a pronounced excursion to low  $\delta^{11}\text{B}$  values around 16.5-14 kyrBP. The record from core PC83-1 spans the last 16 kyr (Figure 3e). In this core, the  $\delta^{11}\text{B}$  values in both the early deglacial section and the Holocene section are close to 15-15.5‰, while values from the late deglacial section and the core top are characterized by values of ~16‰. Once converted to pH (Figure 3c, g) these records demonstrate the surface/shallow subsurface pH in the SW Pacific was ~8.2 during the LGM and early deglaciation, before being punctuated by low pH values between ~16.5-14 kyrBP (Figure 3c). pH values are around ~8.1 in the late deglaciation and early Holocene and rise to 8.2 at the core top (~2.3 kyrBP). The pCO<sub>2</sub>

reconstruction at our site suggests on Chatham Rise, sea surface  $p\text{CO}_2$  were up to ~300 to 450  $\mu$  atm during the last deglaciation and early Holocene.

### 3.2 pH and Seawater $p\text{CO}_2$ Composite vs the Simulated GMSSpH

Table 3 summarizes the estimated  $\text{pH}_{\text{boron\_Holocene}}$ ,  $\text{pH}_{\text{site\_preind}}$ ,  $p\text{CO}_{2\text{boron\_Holocene}}$  and  $p\text{CO}_{2\text{site\_preind}}$  for 12 individual records. Based on these estimations, the ‘location bias’ and the ‘reconstruction bias’ are corrected. Individual pH records are shown against the composite pH in Figure 4. The pH and  $p\text{CO}_2$  composite are built on 219 boron isotope data from 12 cores sites (Figure 5a, 5b). pH values from ODP999 closely follows the median composite, while in most other cases, an individual record generally fluctuates around the median composite, with a few data points falling outside of the 95% envelop of the composite (Figure 4). Some recognizable patterns are: 1) During the LGM and early deglaciation (25-15 kyrBP), the ODP1238 record consistently shows higher pH, while the GeoB1105 record shows lower pH than the composite; 2) AAS9, NIOP464, PC75-2, EDRC92 and MD01-2416 all show anomalously low pH values between 15-14 kyrBP; 3) During the late deglaciation (15-10 kyrBP), although some data points from GeoB1523, GeoB1105 and PC83-1 are close to the composite, other pH values are higher than the composite mean. We emphasize here again that the above description is based on corrected pH values (i.e.  $\text{pH}_{\text{final}}$ ) in this study, which should not be confused with conclusions drawn from uncorrected pH values (e.g. section 3.1 for our data and original publications for other records.). For reference, individual uncorrected pH records (i.e.  $\text{pH}_{\text{boron}}$ ) are plotted with the composite in Figure S5.

The composites are developed from 12 cores that come from a wide range of oceanographic settings. At sites where the carbonate system is strongly affected by seasonality

and the fluxes of planktic foraminiferal tests have distinct seasonal patterns, the pH and thus  $p\text{CO}_2$  estimates will likely be biased towards the season of maximum production. Also, since foraminifers calcify over a range of depths instead of strictly at the surface, the composite may be biased towards higher  $p\text{CO}_2$  because sea-water  $p\text{CO}_2$  increases with depth within the top few hundreds of meters (Ezat et al., 2017; Raitzsch et al., 2018; Taylor et al., 2018; Yu et al., 2013). However, we found that these complexities would only have minor effects on our composite  $p\text{CO}_2$  (Figure S6, S7), probably because the calibrations that are largely based on core top measurements that already account for some of these effects.

Three scenarios of simulated GMSSpH over the last 25 kyr are presented in Figure 5c; these curves follow the same deglacial structure, due to the close coupling between  $p\text{CO}_2$  and surface ocean pH, but have different absolute values, due to their different alkalinity and DIC (Table 2). For a given  $p\text{CO}_2$ , DIC removal results in slightly lower pH than alkalinity addition, while addition of alkalinity and DIC in a 2:1 ratio ( $\text{CaCO}_3$  addition) gives higher pH with a larger offset, due to the larger change in ALK-DIC chemistry in this scenario. Our three scenarios provide different end member GMSSpH solutions for glacial  $p\text{CO}_2$ , and the real sea surface carbonate chemistry condition at the LGM and thus the real deglacial GMSSpH evolution likely falls in the range of the three curves in Figure 5c. The  $\delta^{11}\text{B}$ -derived pH and  $p\text{CO}_2$  composites match the overall trend of the GMSSpH simulated by cGENIE and the atmospheric record of  $p\text{CO}_2$ , respectively (Figure 5b, c, Table S6). However, during the last deglaciation, the composite pH is generally lower than all three simulated GMSSpH, and, correspondingly, the composite  $p\text{CO}_2$  is generally higher than the contemporary atmosphere.  $p\text{CO}_2$  disequilibrium in the deglaciation is quite robust, given that this interval has the best data coverage, and the lower 2.5% quantile also falls above the atmospheric  $p\text{CO}_2$  record (Figure 5b).

## 4. Discussion

### 4.1 Chatham Rise as a Source of Carbon to the Atmosphere over the Last 19 kyr.

Results presented in this study indicate that the subtropical-subpolar transition zone of the SW Pacific was a site of carbon ventilation during the last deglaciation (Figure 6a), whereas in the modern ocean this region is a modest carbon sink (Figure 1a, Figure S1). A similar result was observed at a South Atlantic site (Martínez-Botí et al., 2015) that is also a sink region in the modern ocean. Together, these results suggest that both the Atlantic and Pacific sectors of the Southern Ocean became sources of CO<sub>2</sub> to the atmosphere during the deglaciation.

We acknowledge that our cores are of low resolution, therefore the two records may not resolve the complete history of surface  $\Delta p\text{CO}_2$  in this region. We note that for many time intervals we do not have overlapping data from both cores, thus it is not possible to rule out that the offsets seen between the two cores may represent higher-frequency variability than is captured by the resolution of each core. There are also mismatches in reconstructed pH/ $\Delta p\text{CO}_2$  at apparently overlapping time intervals between the two records, but due to age model uncertainties (note there are only 3 radiocarbon dates to constrain the age model of PC83-1, see the magenta triangle markers in Figure 3 and 6) and low resolution, it is possible that these intervals of apparent mismatch do not truly represent overlapping time intervals, as evidenced by some notable differences in Mg/Ca -based SST between these records. With the above caveats in mind, we now discuss the main signals in the boron isotope data in context with other paleoceanographic proxies in this region.

#### 4.1.1 Possible geological carbon influence on our site on Chatham Rise

Two cores from Chatham Rise document extreme negative benthic  $\Delta^{14}\text{C}$  values between 2000-3000m at the last glacial termination (Ronge et al., 2016). Ronge et al., (2016)

hypothesized that these sites record the influence of radiocarbon-dead hydrothermal CO<sub>2</sub> transported from the East Pacific Rise. However, it is unlikely that such large  $\Delta^{14}\text{C}$  anomalies from volcanic degassing of CO<sub>2</sub> from the East Pacific Rise would reach Chatham Rise without losing their highly <sup>14</sup>C-depleted radiocarbon signature (Ronge et al., 2016). Also, there are no known hydrothermal systems near Chatham Rise that could provide such <sup>14</sup>C-depleted carbon.

Large pockmarks have been identified across the southern edge of the Chatham Rise in seismic sections (Davy et al., 2010), close to the cores that document large negative  $\Delta\Delta^{14}\text{C}$  anomalies (this study and Ronge et al., 2015). Davy et al., (2010) previously hypothesized that the pockmarks formed at glacial terminations during the Pleistocene and argued that they came about in response to destabilization of methane hydrates. A subsequent research cruise was conducted in 2013 to explore for methane hydrates but none of the data from that investigation support there being a flux of methane through the sediment (Coffin et al., 2013), which suggests the pockmarks formed in response to release of old geologic CO<sub>2</sub> rather than CH<sub>4</sub> (Stott et al., in revision). It appears from seismic profiles that pockmarks have recurred through the Pleistocene and therefore there have been recurrent episodes of geologic carbon release through these pockmarks on the Chatham Rise during earlier glacial cycles. Our PC75 core was taken in close proximity to one of the large pockmarks as was the core studied by Ronge et al., (2016).

Today, our PC75 core site is bathed by well-ventilated, relatively ‘young’ AAIW. However, between 25-16 kyrBP, the benthic radiocarbon values were much more depleted compared to the contemporaneous atmosphere ( $\Delta\Delta^{14}\text{C}$  of ~300-400‰; Figure 6c). This atmosphere-benthic  $\Delta^{14}\text{C}$  offset is much larger than values from corals collected at slightly deeper water depths in the Tasman Sea (Hines et al., 2015) (regardless of our assumptions about surface reservoir ages, see Figure S8). These data, together with the results of Ronge et al.,

(2016), indicate there were local sources of much older carbon at the Chatham Rise between 25-16 kyrBP.

Our boron isotope data only extends to 20 kyr. Over this period  $\Delta p\text{CO}_2$  values range between 0-80ppm in the PC75-2 record. It is possible that some of the old carbon that was responsible for the benthic  $\Delta^{14}\text{C}$  excursions reached surface waters, which could account for the elevated surface ocean  $p\text{CO}_2$  and the anomalously old surface reservoir ages (Sikes & Guilderson, 2016; Skinner et al., 2015) (see a conceptual diagram for the LGM, Figure 7b). This idea will require additional evaluation but the fact that the pockmarks, the  $\Delta^{14}\text{C}$  anomalies, including those documented by Ronge et al., (2016), and elevated  $p\text{CO}_2$  values coincided suggest they may have been mechanistically linked. And the fact that the atmosphere-benthic  $\Delta\Delta^{14}\text{C}$  values remained low for several thousand years further suggests there was a substantial and relatively continuous supply of old carbon and perhaps reduced ventilation between 900-2500m of the SW Pacific that prolonged the  $\Delta\Delta^{14}\text{C}$  anomaly during the early deglaciation.

#### **4.1.2 Surface Ocean $p\text{CO}_2$ , 16.5-14 kyr**

The interval from 16.5-14 kyrBP is characterized by the most prominent  $\text{CO}_2$  outgassing event in our reconstruction (Figure 6a, shaded in yellow). There are five data points from the two records that suggest the surface  $\Delta p\text{CO}_2$  was up to +100ppm during this period. Notably, the peak outgassing coincided with periods of rapidly rising atmospheric  $\text{CO}_2$  (~16.3 and 14.8 kyrBP) (Marcott et al., 2014) (Figure 6d). This outgassing event at the surface is also closely associated with a rapid rise in carbonate ion saturation at mid depths of the Southwest Pacific (Allen et al., 2015) (Figure 6b) and thus, an apparent loss of carbon from mid-depth deep waters (assuming that alkalinity is unlikely to change this dramatically). At the same time, benthic  $\Delta\Delta^{14}\text{C}$  (this study; Ronge et al., 2016) returned to younger (Figure 6c, see Table S7 for the  $\Delta^{14}\text{C}$  data),

Holocene-like values, suggesting enhanced ventilation of the intermediate depths of the Southwest Pacific.

Between 16.5-14 kyrBP, there was a rapid 0.5‰ increase in benthic  $\delta^{13}\text{C}$  values, followed by a 0.3‰ decline at our site. This pattern is also observed in the MD97-2120 and 79JPC records from the SW Pacific and the MD07-3088 record from the Southeast Pacific, although the magnitude of  $\delta^{13}\text{C}$  drop differs among these records (Figure S9a) and in some other cores is much less pronounced (Figure S9b). Given the rapidity of this transient benthic  $\delta^{13}\text{C}$  event, previous authors attributed this positive  $\delta^{13}\text{C}$  event to changes in ventilation and/or water mass structure driven by changes in winds or buoyancy forcing (Ronge et al., 2015; Sikes et al., 2016) in the SW Pacific. More specifically, during late HS1 when the Southern Hemisphere warmed, enhanced upwelling (Anderson et al., 2009) and a southward shift in the westerlies (Lamy et al., 2010; Putnam et al., 2010) and the sea ice edge (Ferrari et al., 2014; Rae et al., 2018) would have flushed respired carbon from these mid-depth waters (Jaccard et al., 2016; Rae et al., 2018) and/or supplied positive  $\delta^{13}\text{C}$  to these layers, due to enhanced air-sea gas exchange in the Southern Ocean. The reverse (i.e. reduced ventilation of intermediate waters) would have occurred during the Antarctic Cold Reversal (ACR), a period of SH cooling. A deepening (shoaling) of the AAIW/CDW boundary during late HS1 (ACR) may also contribute to this pattern (Figure S9).

However, there are also some differences in the nature of the deglacial benthic  $\delta^{13}\text{C}$  signal from this region that may point to some added complexities (Figure S9b). For instance, some records are characterized by a more gradual increase in  $\delta^{13}\text{C}$ , ranging from 0.3-0.6‰ between 16.5-14 kyrBP, without any significant drop after HS1. It is possible that the temporal resolutions of some records (e.g. SO136-003 and SO213-84) are not high enough to capture the



full  $\delta^{13}\text{C}$  excursion. The potential influence of localized geological sources of  $\text{CO}_2$  may also influence some of the records and introduce additional complexity to interpretation of benthic  $\delta^{13}\text{C}$  records in this region. Direct observations of the  $\delta^{13}\text{C}$  signature of the carbon coming from geological systems is crucial to improve our understanding of the benthic  $\delta^{13}\text{C}$  from this region. A full investigation of benthic  $\delta^{13}\text{C}$  records from intermediate depths is beyond the scope of the current study but has the potential to shed further light on these processes.

Notwithstanding the complexities described above, the large outgassing event between 16.5-14 kyrBP, documented by our new boron isotope data, was associated with a rapid increase in bottom water  $[\text{CO}_3^{2-}]$ , benthic  $\delta^{13}\text{C}$  and  $\Delta\Delta^{14}\text{C}$  increase, as well as high opal fluxes in the Southern Ocean, that would have accompanied release of respired - and possibly also geological - carbon from intermediate depths of the South Pacific, probably through a general enhancement of ocean ventilation relative to the glacial period. Taking our reconstructed  $\Delta\text{pCO}_2$  at face value, the data imply substantial carbon transfer from intermediate depths of the South Pacific to the upper ocean and eventually to the atmosphere between ~16.5-14 kyrBP.

#### **4.2 Positive Air-Sea $\Delta\text{pCO}_2$ Anomalies during the deglaciation and early Holocene**

The median composite  $\Delta\text{pCO}_2$  curve shows a positive excursion of up to 50 ppm during the last deglaciation, and more subtle positive excursions during the early Holocene (Figure 8e). Given the potential caveats of our new data, we also present a second composite that excludes the two records from Chatham Rise (Figure S10). Between 14-15 kyrBP and 5-10 kyrBP,  $\Delta\text{pCO}_2$  from the second composite is lower than the first one by ~10ppm. However, excluding the two records from Chatham Rise in the composite does not change the first order picture - the composite

$\Delta p\text{CO}_2$  shows a positive anomaly over the last deglaciation and in the early Holocene, providing direct evidence that the ocean released carbon to the atmosphere at these times.

The deglacial  $\Delta p\text{CO}_2$  pulse is the most statistically significant, with the lower 2.5% quantile being above the equilibrium line (Figure 8e). This highlights the importance of ocean  $\text{CO}_2$  outgassing for atmospheric  $p\text{CO}_2$  rise during the last deglaciation. Although it is difficult to constrain how much area of the ocean each individual core represents, it appears that the deglacial  $\Delta p\text{CO}_2$  and presumably oceanic  $\text{CO}_2$  outgassing flux encompassed a broader part of the global surface ocean than the just the areas typically thought of as key for  $\text{CO}_2$  outgassing. However, note that for each 1000-year bin, there are roughly equal amounts of data from upwelling sites and non-upwelling sites (Figure 8f), whereas upwelling regions only occupy a relatively small amount of the global surface ocean area. These areas are connected to carbon in the deep and abyssal ocean and therefore were more likely to release extra carbon during the deglaciation. Interestingly, the site of PC75/83 and PS2498-1, both located in a moderate sink region today, appear to be a source of carbon over the last deglaciation, perhaps due to frontal shifts (Barker et al., 2009; Bostock et al., 2015) and/or stronger upwelling in the Southern Ocean (Anderson et al., 2009). Such transitions are not taken into account by correcting the ‘location bias’, but importantly, they are likely to reveal real signals of oceanic carbon cycle perturbations. Our results highlight a need to constrain the oceanic sink regions to better understand the complete history of air-sea  $\text{CO}_2$  exchange over the last deglaciation.

$\Delta p\text{CO}_2$  values in the late deglacial and early Holocene are also elevated, notably at a time of little change in atmospheric  $p\text{CO}_2$ . This may be explained if ocean  $\text{CO}_2$  outgassing at this time is partially compensated by expansion of carbon sinks. The most likely candidate is regrowth of the terrestrial biosphere, which would also contribute to the increase in  $\delta^{13}\text{C}$  in the deep ocean

and the atmosphere at this time (Figure 8b). Thus, a substantial portion of the CO<sub>2</sub> released from the ocean during the late deglacial and early Holocene was probably being absorbed by terrestrial vegetation instead of remaining in the atmosphere, as previously suggested based on an increase in deep ocean carbonate ion concentration (Yu et al., 2010). There is also a significant peak in  $\Delta p\text{CO}_2$  in the mid Holocene, at a time of relatively stable  $\delta^{13}\text{C}$  and gradually rising CO<sub>2</sub>. This may be driven in part by CO<sub>2</sub> released from renewed shallow water CaCO<sub>3</sub> deposition (Ridgwell et al., 2003) as sea levels rose (Spratt & Lisiecki, 2016) (Figure 8c), alongside carbonate compensation at depth (Broecker & Clark, 2007).

The interpretations presented here remain limited by a sparse sampling of the global ocean and age model uncertainties. Another caveat is the net exchange of carbon between the global ocean and the atmosphere depends not only on global mean  $\Delta p\text{CO}_2$ , but also on the local CO<sub>2</sub> gas exchange rates governed by wind speed, which has not been quantitatively constrained here. Future work to increase the spatial and temporal resolution of planktic  $\delta^{11}\text{B}$ -based pH and CO<sub>2</sub> reconstructions, particularly in sink regions, and a better understanding of mechanisms responsible for the complex pattern of air-sea CO<sub>2</sub> exchange in different parts of the global Ocean, is essential to advancing our understanding of glacial/interglacial CO<sub>2</sub> variability.

## 5 Conclusions

We have added two new boron isotope records to the existing archive, partly filling an important spatial data gap in the subtropical-subpolar transition zone of the SW Pacific. Composite records of pH and pCO<sub>2</sub> were also compiled and reanalyzed from 12 sites that reveal intriguing patterns of ocean/atmosphere disequilibrium that may reflect a spatially and

temporally complex history of CO<sub>2</sub> ventilation across the last 25 kyr. Based on results presented here we conclude the following:

1) New boron isotope-based pH records for the subtropical-subpolar South Pacific indicates the Chatham Rise was a source of carbon to the ocean/atmosphere during the last deglaciation. We suggest that respired carbon, and possibly geological carbon, from this region was ventilated through the Southern Ocean to the atmosphere between 16.5-14 kyrBP. However, there are mismatches in reconstructed pH/pCO<sub>2</sub> and SST between the two records that put a question mark on how representative these records are of wider oceanographic processes.

2) The composite pH derived from 12 boron isotope records throughout the global ocean agrees well with simulated GMSSpH by cGENIE and captures the first-order deglacial trend. The composite pCO<sub>2</sub> reveals pronounced ocean outgassing to the atmosphere from a broad part of the global surface ocean during the last deglaciation and early Holocene, although the sites included in the composite might be biased towards upwelling regions. Future work on reconstructing pCO<sub>2</sub> from sink regions is required to fully evaluate the dynamic history of air-sea exchange of CO<sub>2</sub>. During the late deglaciation and early Holocene oceanic outgassing of CO<sub>2</sub> could partially be compensated by regrowth of terrestrial vegetation and carbonate compensation in the deep ocean.

## **Acknowledgments**

The authors wish to express their appreciation for the analytical support provided by the Keck Carbon Cycle Accelerator Mass Spectrometry Laboratory. We thank Gavin Foster and Andy Ridgwell for constructive conversations. J. Shao and L.D. Stott were supported by an NSF grant

(MG&G 1558990). W. R. Gray and R. Greenop were supported by NERC grants NE/N011716/1 and NE/N011716/1 to J.W.B. Rae. I. Pecher, H.L. Neil, and B. Davy were supported by RSNZ Marsden Fund grant UOA1022. R. Coffin was supported by a DOE-NETL contract to NRL subcontract to TAMUCC (#601970). All data are available as supporting information to this paper.

## References:

- Allen, K. A., Sikes, E. L., Hönisch, B., Elmore, A. C., Guilderson, T. P., Rosenthal, Y., & Anderson, R. F. (2015). Southwest Pacific deep water carbonate chemistry linked to high southern latitude climate and atmospheric CO<sub>2</sub> during the Last Glacial Termination. *Quaternary Science Reviews*, 122, 180–191.  
<https://doi.org/10.1016/j.quascirev.2015.05.007>
- Anderson, R. F., Ali, S., Bradtmiller, L. I., Nielsen, S. H. H., Fleisher, M. Q., Anderson, B. E., & Burckle, L. H. (2009). Wind-Driven Upwelling in the Southern Ocean and the Deglacial Rise in Atmospheric CO<sub>2</sub>. *Science*, 323(5920), 1443–1448.  
<https://doi.org/10.1126/science.1167441>
- Barker, S., Greaves, M., & Elderfield, H. (2003). A study of cleaning procedures used for foraminiferal Mg/Ca paleothermometry. *Geochemistry, Geophysics, Geosystems*, 4(9).  
<https://doi.org/10.1029/2003GC000559>
- Barker, Stephen, Diz, P., Vautravers, M. J., Pike, J., Knorr, G., Hall, I. R., & Broecker, W. S. (2009). Interhemispheric Atlantic seesaw response during the last deglaciation. *Nature*, 457(7233), 1097–1102. <https://doi.org/10.1038/nature07770>

- Basak, C., Fröllje, H., Lamy, F., Gersonde, R., Benz, V., Anderson, R. F., et al. (2018). Breakup of last glacial deep stratification in the South Pacific. *Science*, 359(6378), 900–904. <https://doi.org/10.1126/science.aao2473>
- Bereiter, B., Eggleston, S., Schmitt, J., Nehrbass-Ahles, C., Stocker, T. F., Fischer, H., et al. (2015). Revision of the EPICA Dome C CO<sub>2</sub> record from 800 to 600 kyr before present: Analytical bias in the EDC CO<sub>2</sub> record. *Geophysical Research Letters*, 42(2), 542–549. <https://doi.org/10.1002/2014GL061957>
- Bostock, H. C., Hayward, B. W., Neil, H. L., Sabaa, A. T., & Scott, G. H. (2015). Changes in the position of the Subtropical Front south of New Zealand since the last glacial period. *Paleoceanography*, 30(7), 824–844. <https://doi.org/10.1002/2014PA002652>
- Broecker, W., & Clark, E. (2007). Is the magnitude of the carbonate ion decrease in the abyssal ocean over the last 8 kyr consistent with the 20 ppm rise in atmospheric CO<sub>2</sub> content?: HOLOCENE DECREASE IN DEEP-SEA CARBONATE. *Paleoceanography*, 22(1), n/a-n/a. <https://doi.org/10.1029/2006PA001311>
- Cao, L., Eby, M., Ridgwell, A., Caldeira, K., Archer, D., Ishida, A., et al. (2009). The role of ocean transport in the uptake of anthropogenic CO<sub>2</sub>. *Biogeosciences*, 6(3), 375–390. <https://doi.org/10.5194/bg-6-375-2009>
- Chase, Z., Anderson, R. F., Fleisher, M. Q., & Kubik, P. W. (2003). Accumulation of biogenic and lithogenic material in the Pacific sector of the Southern Ocean during the past 40,000 years. *Deep Sea Research Part II: Topical Studies in Oceanography*, 50(3–4), 799–832. [https://doi.org/10.1016/S0967-0645\(02\)00595-7](https://doi.org/10.1016/S0967-0645(02)00595-7)
- Coffin, R. B., Boyd, T. J., Rose, P. S., Yoza, B., Millholland, L. C., Downer, R., & Woods, S. (2013). *Geochemical Cruise Report SO226/2 RV Sonne Chatham Rise Expedition: Fort*

Belvoir, VA: Defense Technical Information Center.

<https://doi.org/10.21236/ADA587416>

Davy, B., Pecher, I., Wood, R., Carter, L., & Gohl, K. (2010). Gas escape features off New Zealand: Evidence of massive release of methane from hydrates: MASSIVE NZ GAS ESCAPE FEATURES. *Geophysical Research Letters*, 37(21).

<https://doi.org/10.1029/2010GL045184>

Dickson, A. G. (1990). Thermodynamics of the dissociation of boric acid in synthetic seawater from 273.15 to 318.15 K. *Deep Sea Research Part A. Oceanographic Research Papers*, 37(5), 755–766. [https://doi.org/10.1016/0198-0149\(90\)90004-F](https://doi.org/10.1016/0198-0149(90)90004-F)

Edgar, K. M., Anagnostou, E., Pearson, P. N., & Foster, G. L. (2015). Assessing the impact of diagenesis on  $\delta^{11}\text{B}$ ,  $\delta^{13}\text{C}$ ,  $\delta^{18}\text{O}$ , Sr/Ca and B/Ca values in fossil planktic foraminiferal calcite. *Geochimica et Cosmochimica Acta*, 166, 189–209.

<https://doi.org/10.1016/j.gca.2015.06.018>

Edwards, N. R., & Marsh, R. (2005). Uncertainties due to transport-parameter sensitivity in an efficient 3-D ocean-climate model. *Climate Dynamics*, 24(4), 415–433.

<https://doi.org/10.1007/s00382-004-0508-8>

Evans, D., Wade, B. S., Henahan, M., Erez, J., & Müller, W. (2016). Revisiting carbonate chemistry controls on planktic foraminifera Mg/Ca: implications for sea surface temperature and hydrology shifts over the Paleocene–Eocene Thermal Maximum and Eocene–Oligocene transition. *Climate of the Past*, 12(4), 819–835.

<https://doi.org/10.5194/cp-12-819-2016>

- Ezat, M. M., Rasmussen, T. L., Hönisch, B., Groeneveld, J., & deMenocal, P. (2017). Episodic release of CO<sub>2</sub> from the high-latitude North Atlantic Ocean during the last 135 kyr. *Nature Communications*, 8, 14498. <https://doi.org/10.1038/ncomms14498>
- Farmer, J. R., Hönisch, B., & Uchikawa, J. (2016). Single laboratory comparison of MC-ICP-MS and N-TIMS boron isotope analyses in marine carbonates. *Chemical Geology*, 447, 173–182. <https://doi.org/10.1016/j.chemgeo.2016.11.008>
- Ferrari, R., Jansen, M. F., Adkins, J. F., Burke, A., Stewart, A. L., & Thompson, A. F. (2014). Antarctic sea ice control on ocean circulation in present and glacial climates. *Proceedings of the National Academy of Sciences*, 111(24), 8753–8758. <https://doi.org/10.1073/pnas.1323922111>
- Foster, Gavin L., & Rae, J. W. B. (2016). Reconstructing Ocean pH with Boron Isotopes in Foraminifera. *Annual Review of Earth and Planetary Sciences*, 44(1), 207–237. <https://doi.org/10.1146/annurev-earth-060115-012226>
- Foster, Gavin L., Hönisch, B., Paris, G., Dwyer, G. S., Rae, J. W. B., Elliott, T., et al. (2013). Interlaboratory comparison of boron isotope analyses of boric acid, seawater and marine CaCO<sub>3</sub> by MC-ICPMS and NTIMS. *Chemical Geology*, 358, 1–14. <https://doi.org/10.1016/j.chemgeo.2013.08.027>
- Foster, G.L. (2008). Seawater pH, pCO<sub>2</sub> and [CO<sub>3</sub><sup>2-</sup>] variations in the Caribbean Sea over the last 130 kyr: A boron isotope and B/Ca study of planktic foraminifera. *Earth and Planetary Science Letters*, 271(1–4), 254–266. <https://doi.org/10.1016/j.epsl.2008.04.015>
- Foster, G.L., & Sexton, P. F. (2014). Enhanced carbon dioxide outgassing from the eastern equatorial Atlantic during the last glacial. *Geology*, 42(11), 1003–1006. <https://doi.org/10.1130/G35806.1>



Franois, R., Altabet, M. A., Yu, E.-F., Sigman, D. M., Bacon, M. P., Frank, M., et al. (1997).

Contribution of Southern Ocean surface-water stratification to low atmospheric CO<sub>2</sub> concentrations during the last glacial period. *Nature*, 389(6654), 929–935.

<https://doi.org/10.1038/40073>

Fry, C. H., Tyrrell, T., Hain, M. P., Bates, N. R., & Achterberg, E. P. (2015). Analysis of global surface ocean alkalinity to determine controlling processes. *Marine Chemistry*, 174, 46–57. <https://doi.org/10.1016/j.marchem.2015.05.003>

Gray, W. R., & Evans, D. (2019). Non-thermal influences on Mg/Ca in planktonic foraminifera: A review of culture studies and application to the last glacial maximum.

*Paleoceanography and Paleoclimatology*. <https://doi.org/10.1029/2018PA003517>

Gray, W. R., Rae, J. W. B., Wills, R. C. J., Shevenell, A. E., Taylor, B., Burke, A., et al. (2018). Deglacial upwelling, productivity and CO<sub>2</sub> outgassing in the North Pacific Ocean. *Nature Geoscience*, 11(5), 340–344. <https://doi.org/10.1038/s41561-018-0108-6>

Gray, W. R., Weldeab, S., Lea, D. W., Rosenthal, Y., Gruber, N., Donner, B., & Fischer, G. (2018). The effects of temperature, salinity, and the carbonate system on Mg/Ca in *Globigerinoides ruber* (white): A global sediment trap calibration. *Earth and Planetary Science Letters*, 482, 607–620. <https://doi.org/10.1016/j.epsl.2017.11.026>

Hain, M. P., Sigman, D. M., & Haug, G. H. (2010). Carbon dioxide effects of Antarctic stratification, North Atlantic Intermediate Water formation, and subantarctic nutrient drawdown during the last ice age: Diagnosis and synthesis in a geochemical box model: ATMOSPHERIC CO<sub>2</sub> DURING THE LAST ICE AGE. *Global Biogeochemical Cycles*, 24(4), n/a–n/a. <https://doi.org/10.1029/2010GB003790>

- Haslett, J., & Parnell, A. (2008). A simple monotone process with application to radiocarbon-dated depth chronologies. *Journal of the Royal Statistical Society: Series C (Applied Statistics)*, 57(4), 399–418. <https://doi.org/10.1111/j.1467-9876.2008.00623.x>
- Hemming, N. G., & Hanson, G. N. (1992). Boron isotopic composition and concentration in modern marine carbonates. *Geochimica et Cosmochimica Acta*, 56(1), 537–543. [https://doi.org/10.1016/0016-7037\(92\)90151-8](https://doi.org/10.1016/0016-7037(92)90151-8)
- Henehan, M. J., Rae, J. W. B., Foster, G. L., Erez, J., Prentice, K. C., Kucera, M., et al. (2013). Calibration of the boron isotope proxy in the planktonic foraminifera *Globigerinoides ruber* for use in palaeo-CO<sub>2</sub> reconstruction. *Earth and Planetary Science Letters*, 364, 111–122. <https://doi.org/10.1016/j.epsl.2012.12.029>
- Henehan, M. J., Foster, G. L., Bostock, H. C., Greenop, R., Marshall, B. J., & Wilson, P. A. (2016). A new boron isotope-pH calibration for *Orbulina universa*, with implications for understanding and accounting for ‘vital effects.’ *Earth and Planetary Science Letters*, 454, 282–292. <https://doi.org/10.1016/j.epsl.2016.09.024>
- Hines, S. K. V., Southon, J. R., & Adkins, J. F. (2015). A high-resolution record of Southern Ocean intermediate water radiocarbon over the past 30,000 years. *Earth and Planetary Science Letters*, 432, 46–58. <https://doi.org/10.1016/j.epsl.2015.09.038>
- Hönisch, B., & Hemming, N. G. (2005). Surface ocean pH response to variations in pCO<sub>2</sub> through two full glacial cycles. *Earth and Planetary Science Letters*, 236(1–2), 305–314. <https://doi.org/10.1016/j.epsl.2005.04.027>
- Hönisch, B., Bijma, J., Russell, A. D., Spero, H. J., Palmer, M. R., Zeebe, R. E., & Eisenhauer, A. (2003). The influence of symbiont photosynthesis on the boron isotopic composition of

foraminifera shells. *Marine Micropaleontology*, 49(1–2), 87–96.

[https://doi.org/10.1016/S0377-8398\(03\)00030-6](https://doi.org/10.1016/S0377-8398(03)00030-6)

Huybers, P., & Langmuir, C. (2009). Feedback between deglaciation, volcanism, and atmospheric CO<sub>2</sub>. *Earth and Planetary Science Letters*, 286(3–4), 479–491.

<https://doi.org/10.1016/j.epsl.2009.07.014>

Jaccard, S. L., Galbraith, E. D., Martínez-García, A., & Anderson, R. F. (2016). Covariation of deep Southern Ocean oxygenation and atmospheric CO<sub>2</sub> through the last ice age. *Nature*, 530(7589), 207–210. <https://doi.org/10.1038/nature16514>

Jonkers, L., & Kučera, M. (2015). Global analysis of seasonality in the shell flux of extant planktonic Foraminifera. *Biogeosciences*, 12(7), 2207–2226. <https://doi.org/10.5194/bg-12-2207-2015>

Kırsakürek, B., Eisenhauer, A., Böhm, F., Garbe-Schönberg, D., & Erez, J. (2008). Controls on shell Mg/Ca and Sr/Ca in cultured planktonic foraminiferan, *Globigerinoides ruber* (white). *Earth and Planetary Science Letters*, 273(3–4), 260–269.

<https://doi.org/10.1016/j.epsl.2008.06.026>

Klochko, K., Kaufman, A. J., Yao, W., Byrne, R. H., & Tossell, J. A. (2006). Experimental measurement of boron isotope fractionation in seawater. *Earth and Planetary Science Letters*, 248(1–2), 276–285. <https://doi.org/10.1016/j.epsl.2006.05.034>

Lambeck, K., Rouby, H., Purcell, A., Sun, Y., & Sambridge, M. (2014). Sea level and global ice volumes from the Last Glacial Maximum to the Holocene. *Proceedings of the National Academy of Sciences*, 111(43), 15296–15303. <https://doi.org/10.1073/pnas.1411762111>

Lamy, F., Kilian, R., Arz, H. W., Francois, J.-P., Kaiser, J., Prange, M., & Steinke, T. (2010).

Holocene changes in the position and intensity of the southern westerly wind belt. *Nature Geoscience*, 3(10), 695–699. <https://doi.org/10.1038/ngeo959>

Lauvset, S. K., Key, R. M., Olsen, A., van Heuven, S., Velo, A., Lin, X., et al. (2016). A new global interior ocean mapped climatology: the  $1^\circ \times 1^\circ$  GLODAP version 2, 16.

Lea, D. W., Mashiotto, T. A., & Spero, H. J. (1999). Controls on magnesium and strontium uptake in planktonic foraminifera determined by live culturing. *Geochimica et Cosmochimica Acta*, 63(16), 2369–2379. [https://doi.org/10.1016/S0016-7037\(99\)00197-0](https://doi.org/10.1016/S0016-7037(99)00197-0)

Lowe, D. J., Blaauw, M., Hogg, A. G., & Newnham, R. M. (2013). Ages of 24 widespread tephras erupted since 30,000 years ago in New Zealand, with re-evaluation of the timing and palaeoclimatic implications of the Lateglacial cool episode recorded at Kaipo bog. *Quaternary Science Reviews*, 74, 170–194. <https://doi.org/10.1016/j.quascirev.2012.11.022>

Lund, D. C., Asimow, P. D., Farley, K. A., Rooney, T. O., Seeley, E., Jackson, E. W., & Durham, Z. M. (2016). Enhanced East Pacific Rise hydrothermal activity during the last two glacial terminations. *Science*, 351(6272), 478–482. <https://doi.org/10.1126/science.aad4296>

Marcott, S. A., Bauska, T. K., Buizert, C., Steig, E. J., Rosen, J. L., Cuffey, K. M., et al. (2014). Centennial-scale changes in the global carbon cycle during the last deglaciation. *Nature*, 514(7524), 616–619. <https://doi.org/10.1038/nature13799>

- Martínez-Botí, M. A., Marino, G., Foster, G. L., Ziveri, P., Henehan, M. J., Rae, J. W. B., et al. (2015). Boron isotope evidence for oceanic carbon dioxide leakage during the last deglaciation. *Nature*, 518(7538), 219–222. <https://doi.org/10.1038/nature14155>
- Martinez-Garcia, A., Sigman, D. M., Ren, H., Anderson, R. F., Straub, M., Hodell, D. A., et al. (2014). Iron Fertilization of the Subantarctic Ocean During the Last Ice Age. *Science*, 343(6177), 1347–1350. <https://doi.org/10.1126/science.1246848>
- McCave, I. N., Carter, L., & Hall, I. R. (2008). Glacial–interglacial changes in water mass structure and flow in the SW Pacific Ocean. *Quaternary Science Reviews*, 27(19–20), 1886–1908. <https://doi.org/10.1016/j.quascirev.2008.07.010>
- Monnin, E., Indermuhle, A., Dallenbach, A., Fluckiger, J., Stauffer, B., Stocker, T. F., et al. (2001). Atmospheric CO<sub>2</sub> Concentrations over the Last Glacial Termination. *Science*, 291(5501), 112–114. <https://doi.org/10.1126/science.291.5501.112>
- Naik, S. S., Divakar Naidu, P., Foster, G. L., & Martínez-Botí, M. A. (2015). Tracing the strength of the southwest monsoon using boron isotopes in the eastern Arabian Sea. *Geophysical Research Letters*, 42(5), 1450–1458. <https://doi.org/10.1002/2015GL063089>
- Palmer, M. R., & Pearson, P. N. (2003). A 23,000-Year Record of Surface Water pH and pCO<sub>2</sub> in the Western Equatorial Pacific Ocean. *Science*, 300(5618), 480–482. <https://doi.org/10.1126/science.1080796>
- Palmer, M. R., Brummer, G. J., Cooper, M. J., Elderfield, H., Greaves, M. J., Reichart, G. J., et al. (2010). Multi-proxy reconstruction of surface water pCO<sub>2</sub> in the northern Arabian Sea since 29ka. *Earth and Planetary Science Letters*, 295(1–2), 49–57. <https://doi.org/10.1016/j.epsl.2010.03.023>

- Petit, J. R., Jouzel, J., Raynaud, D., Barkov, N. I., Delaygue, G., Delmotte, M., et al. (1999). Climate and atmospheric history of the past 420,000 years from the Vostok ice core, Antarctica, 399, 8.
- Putnam, A. E., Denton, G. H., Schaefer, J. M., Barrell, D. J. A., Andersen, B. G., Finkel, R. C., et al. (2010). Glacier advance in southern middle-latitudes during the Antarctic Cold Reversal. *Nature Geoscience*, 3(10), 700–704. <https://doi.org/10.1038/ngeo962>
- Rae, J. W. B., Burke, A., Robinson, L. F., Adkins, J. F., Chen, T., Cole, C., et al. (2018). CO<sub>2</sub> storage and release in the deep Southern Ocean on millennial to centennial timescales. *Nature*, 562(7728), 569–573. <https://doi.org/10.1038/s41586-018-0614-0>
- Rae, James W. B. (2018). Boron Isotopes in Foraminifera: Systematics, Biomineralisation, and CO<sub>2</sub> Reconstruction. In H. Marschall & G. Foster (Eds.), *Boron Isotopes: The Fifth Element* (pp. 107–143). Cham: Springer International Publishing. [https://doi.org/10.1007/978-3-319-64666-4\\_5](https://doi.org/10.1007/978-3-319-64666-4_5)
- Rae, James W.B., Foster, G. L., Schmidt, D. N., & Elliott, T. (2011). Boron isotopes and B/Ca in benthic foraminifera: Proxies for the deep ocean carbonate system. *Earth and Planetary Science Letters*, 302(3–4), 403–413. <https://doi.org/10.1016/j.epsl.2010.12.034>
- Raitzsch, M., Bijma, J., Benthien, A., Richter, K.-U., Steinhofel, G., & Kučera, M. (2018). Boron isotope-based seasonal paleo-pH reconstruction for the Southeast Atlantic – A multispecies approach using habitat preference of planktonic foraminifera. *Earth and Planetary Science Letters*, 487, 138–150. <https://doi.org/10.1016/j.epsl.2018.02.002>
- Regenberg, M., Regenberg, A., Garbe-Schönberg, D., & Lea, D. W. (2014). Global dissolution effects on planktonic foraminiferal Mg/Ca ratios controlled by the calcite-saturation state

of bottom waters. *Paleoceanography*, 29(3), 127–142.

<https://doi.org/10.1002/2013PA002492>

Reimer, P. J., Bard, E., Bayliss, A., Beck, J. W., Blackwell, P. G., Ramsey, C. B., et al. (2013).

IntCal13 and Marine13 radiocarbon age calibration curves 0–50000 years cal BP.

*Radiocarbon*, 55(4), 1869–1887. [https://doi.org/10.2458/azu\\_js\\_rc.55.16947](https://doi.org/10.2458/azu_js_rc.55.16947)

Ridgwell, A., Hargreaves, J. C., Edwards, N. R., Annan, J. D., Lenton, T. M., Marsh, R., et al.

(2007). Marine geochemical data assimilation in an efficient Earth System Model of global biogeochemical cycling. *Biogeosciences*, 4(1), 87–104.

Ridgwell, A. J., Watson, A. J., Maslin, M. A., & Kaplan, J. O. (2003). Implications of coral reef buildup for the controls on atmospheric CO<sub>2</sub> since the Last Glacial Maximum.

*Paleoceanography*, 18(4), 1083. <https://doi.org/10.1029/2003PA000893>

Ronge, T. A., Tiedemann, R., Lamy, F., Köhler, P., Alloway, B. V., De Pol-Holz, R., et al.

(2016). Radiocarbon constraints on the extent and evolution of the South Pacific glacial carbon pool. *Nature Communications*, 7, 11487. <https://doi.org/10.1038/ncomms11487>

Ronge, Thomas A., Steph, S., Tiedemann, R., Prange, M., Merkel, U., Nürnberg, D., & Kuhn, G.

(2015). Pushing the boundaries: Glacial/interglacial variability of intermediate and deep waters in the southwest Pacific over the last 350,000 years: Variability in SW-Pacific

AAIW and UCDW. *Paleoceanography*, 30(2), 23–38.

<https://doi.org/10.1002/2014PA002727>

Russell, A. D., Hönisch, B., Spero, H. J., & Lea, D. W. (2004). Effects of seawater carbonate ion concentration and temperature on shell U, Mg, and Sr in cultured planktonic foraminifera.

*Geochimica et Cosmochimica Acta*, 68(21), 4347–4361.

<https://doi.org/10.1016/j.gca.2004.03.013>

- Sanyal, Hemming, N. G., Broecker, W. S., Lea, D. W., Spero, H. J., & Hanson, G. N. (1996). Oceanic pH control on the boron isotopic composition of foraminifera: Evidence from culture experiments. *Paleoceanography*, *11*(5), 513–517.  
<https://doi.org/10.1029/96PA01858>
- Sanyal, Bijma, J., Spero, H., & Lea, D. W. (2001). Empirical relationship between pH and the boron isotopic composition of *Globigerinoides sacculifer*: Implications for the boron isotope paleo-pH proxy. *Paleoceanography*, *16*(5), 515–519.  
<https://doi.org/10.1029/2000PA000547>
- Sikes, E. L., & Guilderson, T. P. (2016). Southwest Pacific Ocean surface reservoir ages since the last glaciation: Circulation insights from multiple-core studies. *Paleoceanography*, *31*(2), 298–310. <https://doi.org/10.1002/2015PA002855>
- Sikes, E. L., Samson, C. R., Guilderson, T. P., & Howard, W. R. (2000). Old radiocarbon ages in the southwest Pacific Ocean during the last glacial period and deglaciation, *405*, 5.
- Sikes, E. L., Elmore, A. C., Allen, K. A., Cook, M. S., & Guilderson, T. P. (2016). Glacial water mass structure and rapid  $\delta^{18}\text{O}$  and  $\delta^{13}\text{C}$  changes during the last glacial termination in the Southwest Pacific. *Earth and Planetary Science Letters*, *456*, 87–97.  
<https://doi.org/10.1016/j.epsl.2016.09.043>
- Skinner, L., McCave, I. N., Carter, L., Fallon, S., Scrivner, A. E., & Primeau, F. (2015). Reduced ventilation and enhanced magnitude of the deep Pacific carbon pool during the last glacial period. *Earth and Planetary Science Letters*, *411*, 45–52.  
<https://doi.org/10.1016/j.epsl.2014.11.024>
- Spratt, R. M., & Lisiecki, L. E. (2016). A Late Pleistocene sea level stack. *Climate of the Past*, *12*(4), 1079–1092. <https://doi.org/10.5194/cp-12-1079-2016>



- Stern, J. V., & Lisiecki, L. E. (2014). Termination 1 timing in radiocarbon-dated regional benthic  $\delta^{18}\text{O}$  stacks. *Paleoceanography*, 29(12), 1127–1142.  
<https://doi.org/10.1002/2014PA002700>
- Stott, L., & Timmermann, A. (2011). Hypothesized Link Between Glacial/Interglacial Atmospheric CO<sub>2</sub> Cycles and Storage/Release of CO<sub>2</sub>-Rich Fluids From Deep-Sea Sediments. In H. Rashid, L. Polyak, & E. Mosley-Thompson (Eds.), *Geophysical Monograph Series* (Vol. 193, pp. 123–138). Washington, D. C.: American Geophysical Union. <https://doi.org/10.1029/2010GM001052>
- Studer, A. S., Sigman, D. M., Martínez-García, A., Benz, V., Winckler, G., Kuhn, G., et al. (2015). Antarctic Zone nutrient conditions during the last two glacial cycles: ANTARCTIC ZONE NUTRIENT CONDITIONS. *Paleoceanography*, 30(7), 845–862.  
<https://doi.org/10.1002/2014PA002745>
- Takahashi, T., Sutherland, S. C., Wanninkhof, R., Sweeney, C., Feely, R. A., Chipman, D. W., et al. (2009). Climatological mean and decadal change in surface ocean pCO<sub>2</sub>, and net sea–air CO<sub>2</sub> flux over the global oceans. *Deep Sea Research Part II: Topical Studies in Oceanography*, 56(8–10), 554–577. <https://doi.org/10.1016/j.dsr2.2008.12.009>
- Taylor, B. J., Rae, J. W. B., Gray, W. R., Darling, K. F., Burke, A., Gersonde, R., et al. (2018). Distribution and ecology of planktic foraminifera in the North Pacific: Implications for paleo-reconstructions. *Quaternary Science Reviews*, 191, 256–274.  
<https://doi.org/10.1016/j.quascirev.2018.05.006>
- Toggweiler, J. R. (1999). Variation of atmospheric CO<sub>2</sub> by ventilation of the ocean's deepest water. *Paleoceanography*, 14(5), 571–588. <https://doi.org/10.1029/1999PA900033>

- Vogl, J., & Rosner, M. (2012). Production and Certification of a Unique Set of Isotope and Delta Reference Materials for Boron Isotope Determination in Geochemical, Environmental and Industrial Materials. *Geostandards and Geoanalytical Research*, 36(2), 161–175. <https://doi.org/10.1111/j.1751-908X.2011.00136.x>
- Yu, J., Thornalley, D. J. R., Rae, J. W. B., & McCave, N. I. (2013). Calibration and application of B/Ca, Cd/Ca, and  $\delta^{11}\text{B}$  in *Neogloboquadrina pachyderma* (sinistral) to constrain  $\text{CO}_2$  uptake in the subpolar North Atlantic during the last deglaciation. *Paleoceanography*, 28(2), 237–252. <https://doi.org/10.1002/palo.20024>
- Zeebe, R. E., Wolf-Gladrow, D. A., Bijma, J., & Hönisch, B. (2003). Vital effects in foraminifera do not compromise the use of  $\delta^{11}\text{B}$  as a paleo- $p\text{H}$  indicator: Evidence from modeling: CRETACEOUS MARINE TEMPERATURE EVOLUTION. *Paleoceanography*, 18(2), n/a-n/a. <https://doi.org/10.1029/2003PA000881>

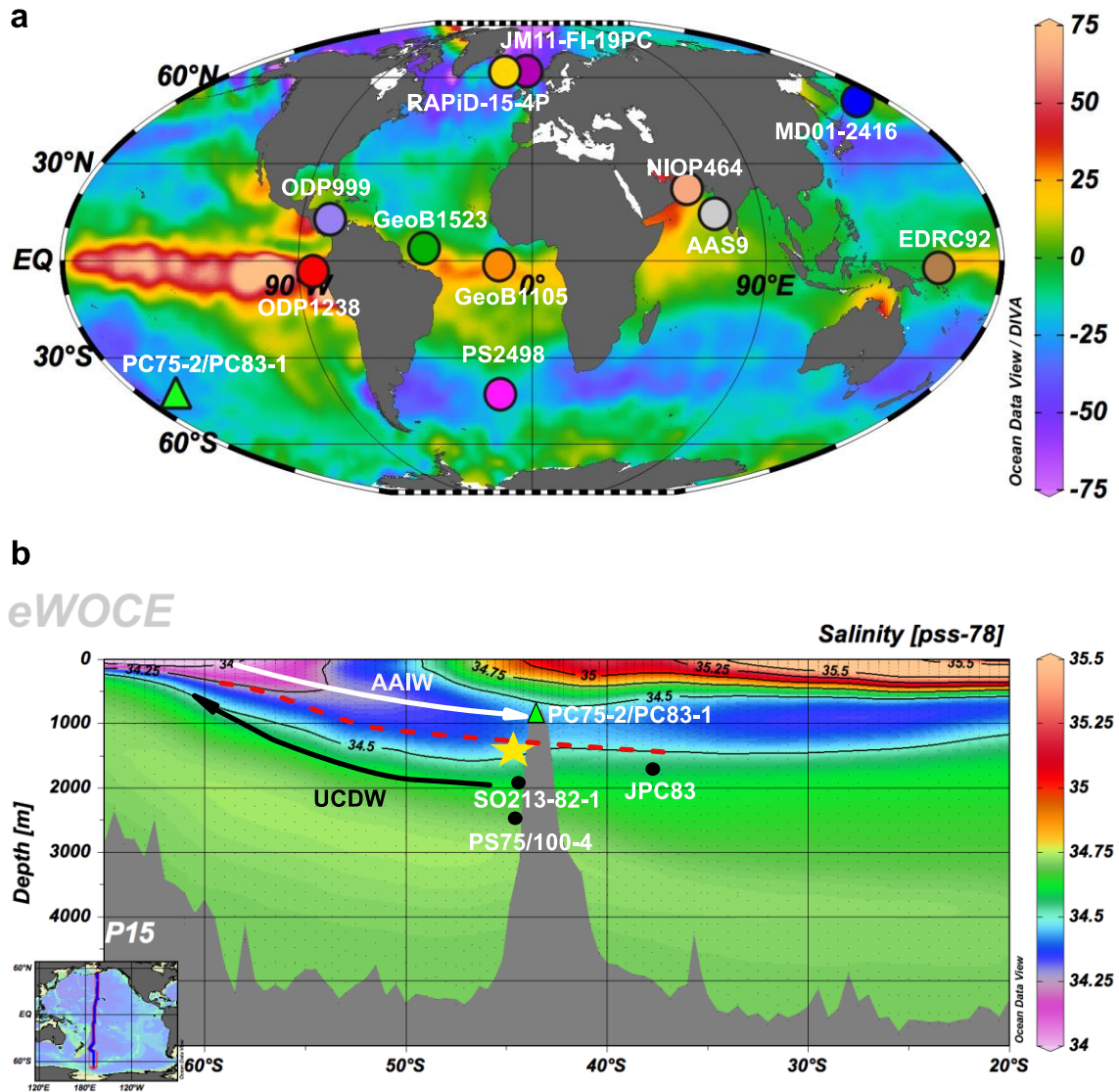


**Figure 1.** (a) Map of mean annual  $\Delta pCO_2$  sea-air. Oceanic sinks and sources are presented by negative and positive  $\Delta pCO_2$  sea-air values (Takahashi et al., 2009), respectively. The green triangle shows the location of the studied sediment cores PC75-2 and PC83-1. The Circles show the locations of the cores with published boron isotope data that span the last deglaciation. (b) Salinity of the P15 transect from the World Ocean Circulation Experiment. The yellow star shows the location of corals (Hines et al., 2015); the black circles show the locations of other

sediment cores (Allen et al., 2015; Ronge et al., 2016) discussed in this study. The red-dotted line marks the boundary between Antarctic Intermediate Water (AAIW) and upper circumpolar Deep Water (UCDW).

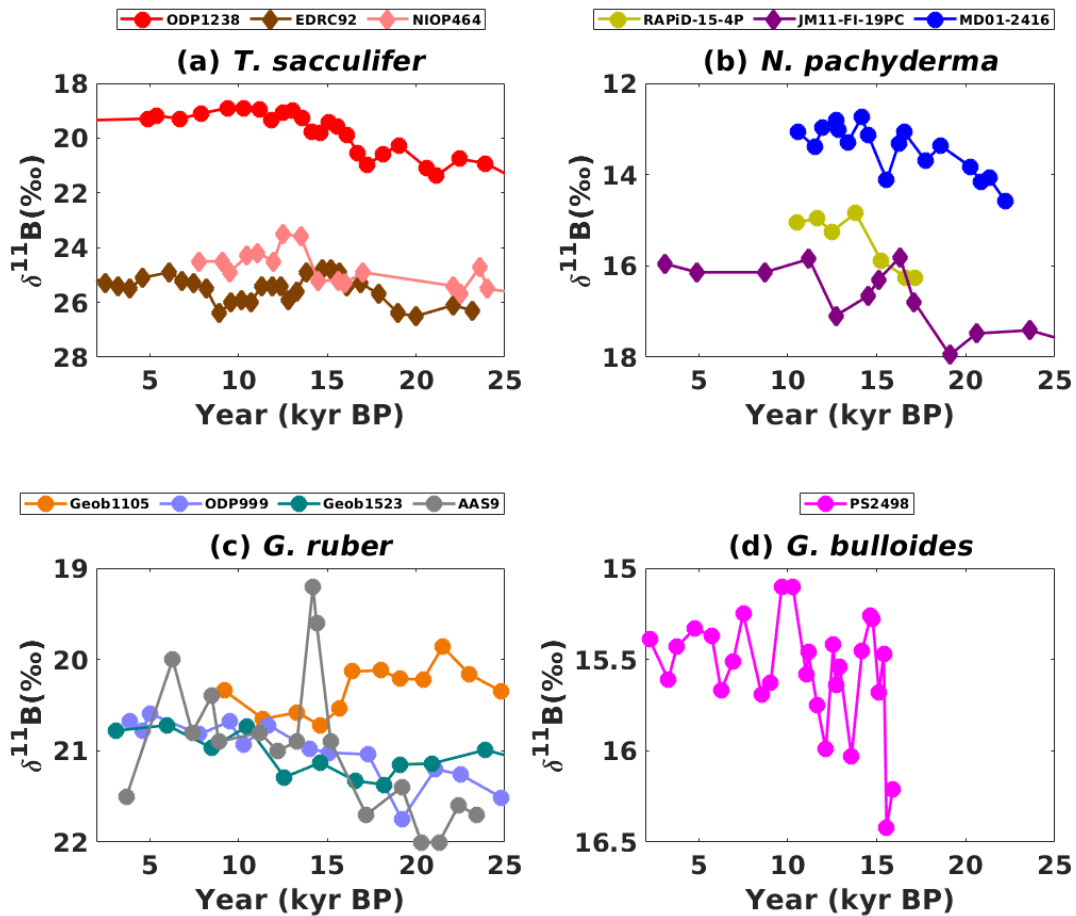


**Figure 2.** 12 published boron records span the last deglaciation grouped into 4 species. (a)  $\delta^{11}\text{B}$  measured in *T. sacculifer*, ODP1238 (red) (Martínez-Botí et al., 2015), EDRC92 (brown) (Palmer & Pearson, 2003) and NIOP464 (pink) (Palmer et al., 2010). (b)  $\delta^{11}\text{B}$  measured in *N. pachyderma*, RAPiD-15-4p (yellow) (Yu et al., 2013), MD01-2416 (blue) (Gray et al., 2018a) and JM11-PI-19PC (dark purple) (Ezat et al., 2017). (c)  $\delta^{11}\text{B}$  measured in *G. ruber*, GeoB1105 (orange) (Foster & Sexton, 2014), ODP999 (light purple) (Foster, 2008), GeoB1523 (dark green) (Foster & Sexton, 2014), ODP999 (light purple) (Foster, 2008), GeoB1523 (dark green) (Foster & Sexton, 2014), ODP999 (light purple) (Foster, 2008), GeoB1523 (dark green) (Foster & Sexton, 2014), ODP999 (light purple) (Foster, 2008), GeoB1523 (dark green) (Foster & Sexton, 2014).

(Henehan et al., 2013) and AAS9 (gray) (Naik et al., 2015). (d)  $\delta^{11}\text{B}$  measured in *G. bulloides* (magenta) (Martínez-Botí et al., 2015). Records generated on a MC-ICPMS are marked with circles and records generated on a NTIMS are marked with diamonds. circles and records.

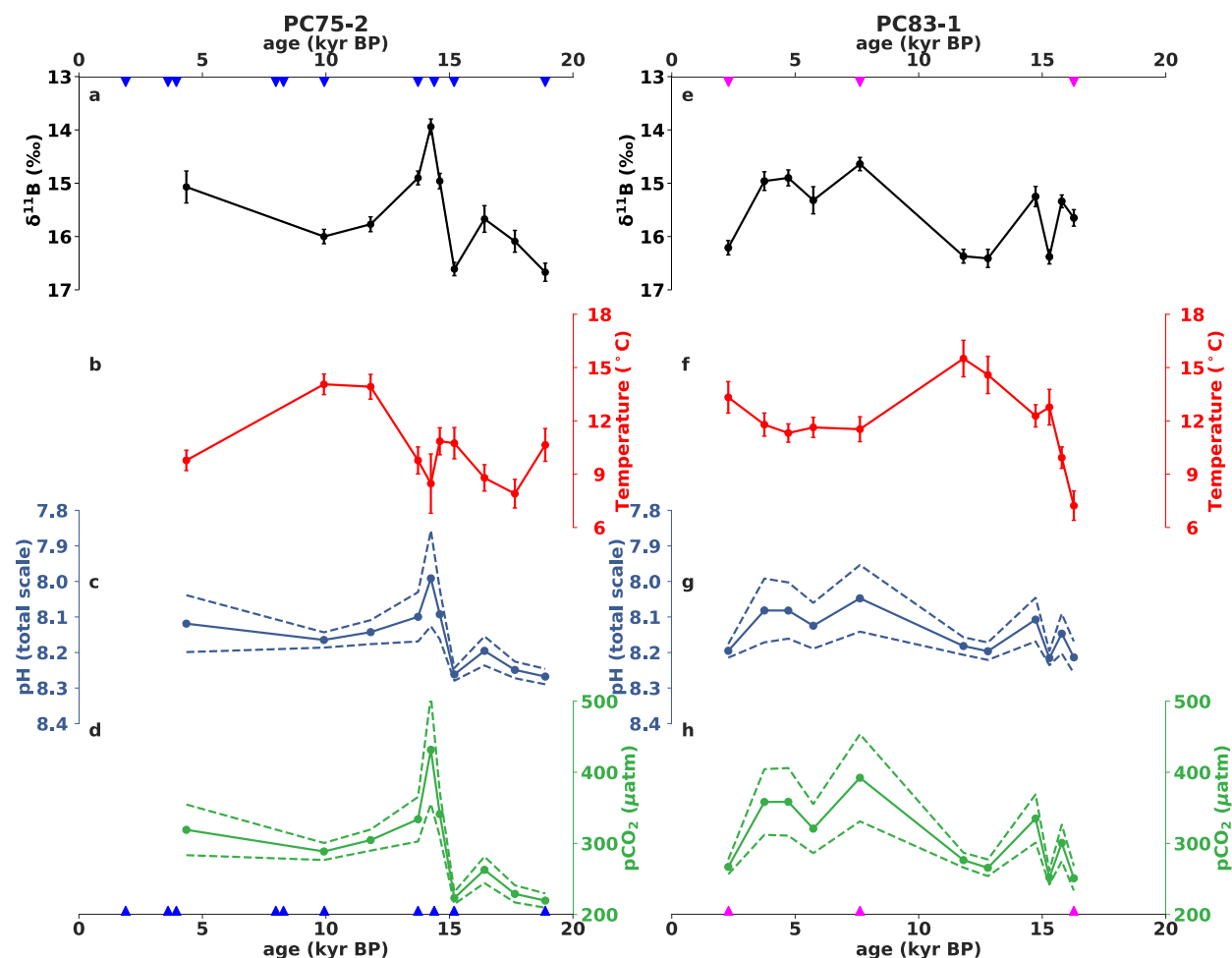


**Figure 3.** Deglacial changes in seawater carbonate chemistry and sea surface temperature of Chatham Rise. a-d, PC75-2; e-h, PC83-1 (a, e) *G. bulloides*  $\delta^{11}\text{B}$  (versus boric acid standard NIST 951) with analytical uncertainties (2 SE). (b, f) *G. bulloides* Mg/Ca-based SST with uncertainties (1 SE) (c, g)  $\delta^{11}\text{B}$ -based pH. (d, h)  $\delta^{11}\text{B}$ -derived  $\text{pCO}_2$ . The dotted envelopes represent uncertainty of sea surface pH and  $\text{pCO}_2$  (1 SE). Triangle marks represent intervals with radiocarbon age constraints.

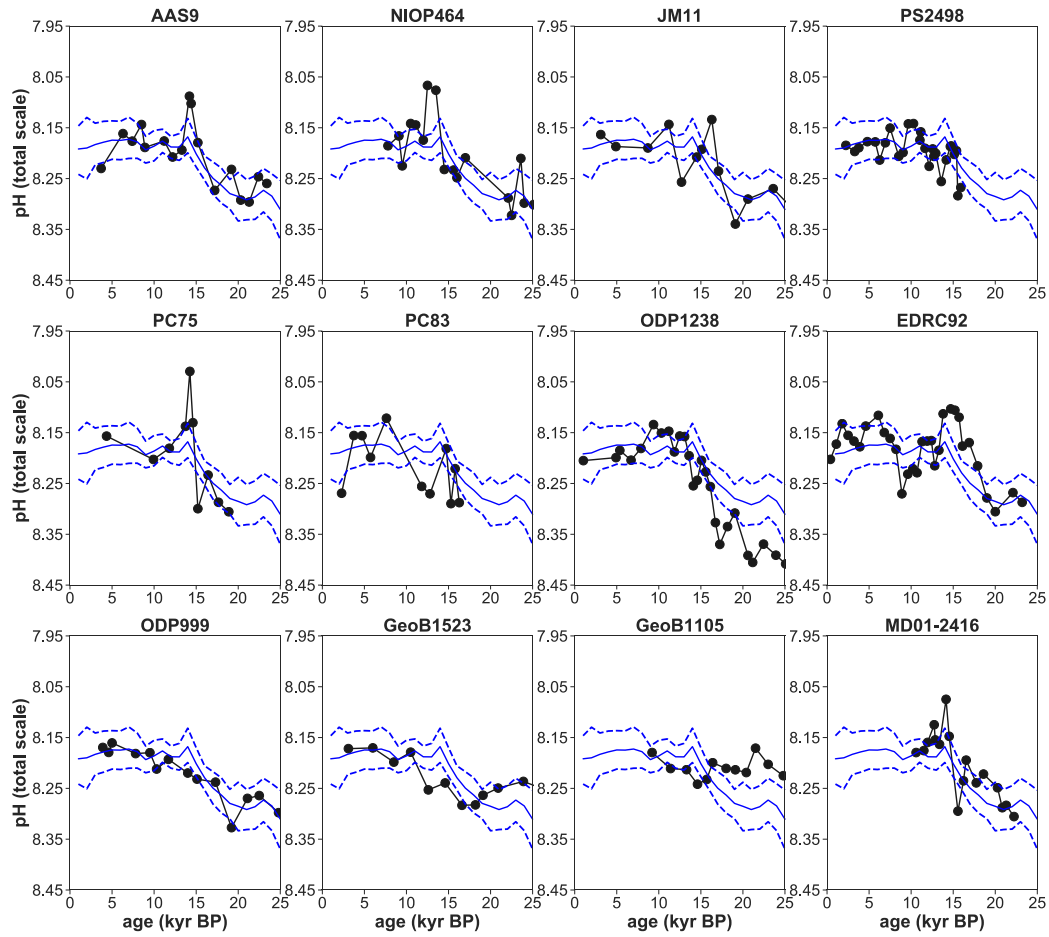


**Figure 4. Individual pH reconstructions (corrected for ‘location bias’, i.e.  $pH_{\text{final}} = pH_{\text{boron}} - pH_{\text{boron\_Holocene}} + pH_{\text{global\_preind}}$ ) plotted against the composite pH.**

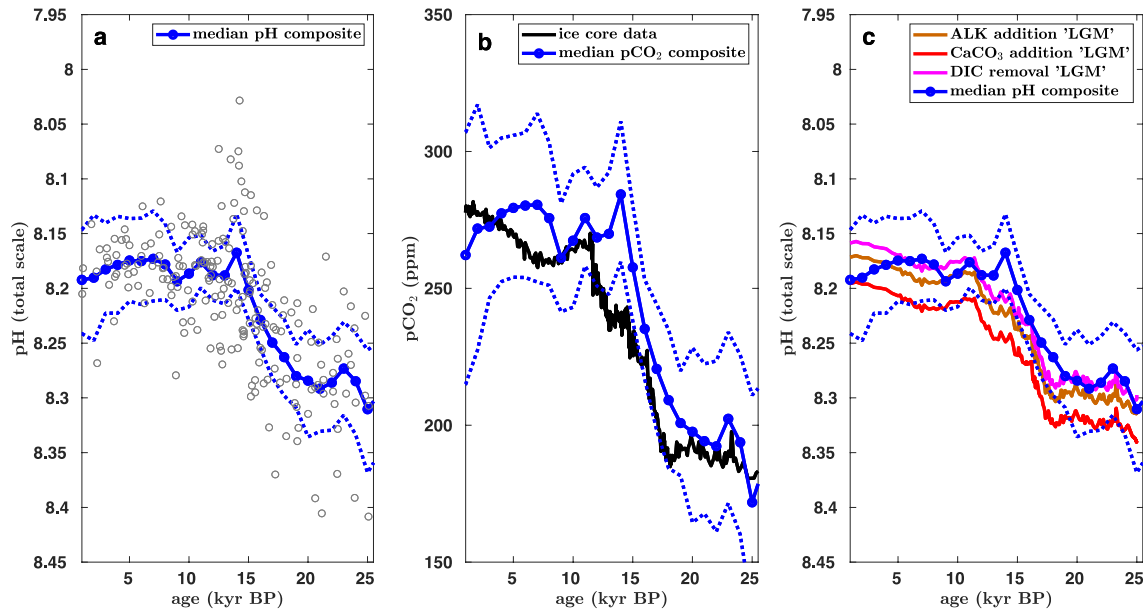


**Figure 5.** composite pH and pCO<sub>2</sub>. a) The solid blue line denotes the median of the 10,000 simulations of the composite pH values. The dotted blue line denotes the 95% quantiles of the 10,000 simulations of the composite pH values. The grey dots represent individual boron isotope derived pH (n=219) after corrections (i.e. pH<sub>final</sub>). b) composite seawater pCO<sub>2</sub> versus the ice core record of atmospheric CO<sub>2</sub>. The solid blue line denotes the median of the 10,000 composite pCO<sub>2</sub>. The dot blue line denotes the 95% quantile of the 10,000 composite pCO<sub>2</sub>. The solid black line represents the ice core record of atmospheric pCO<sub>2</sub>. c) composite pH versus cGENIE inverted pH. The blue lines are the same as in panel a); The solid brown, red, and magenta lines denote the cGENIE simulated GMSSpH evolution where the initial conditions are achieved through ‘ALK addition’, ‘CaCO<sub>3</sub> addition’ and ‘DIC removal’, respectively.

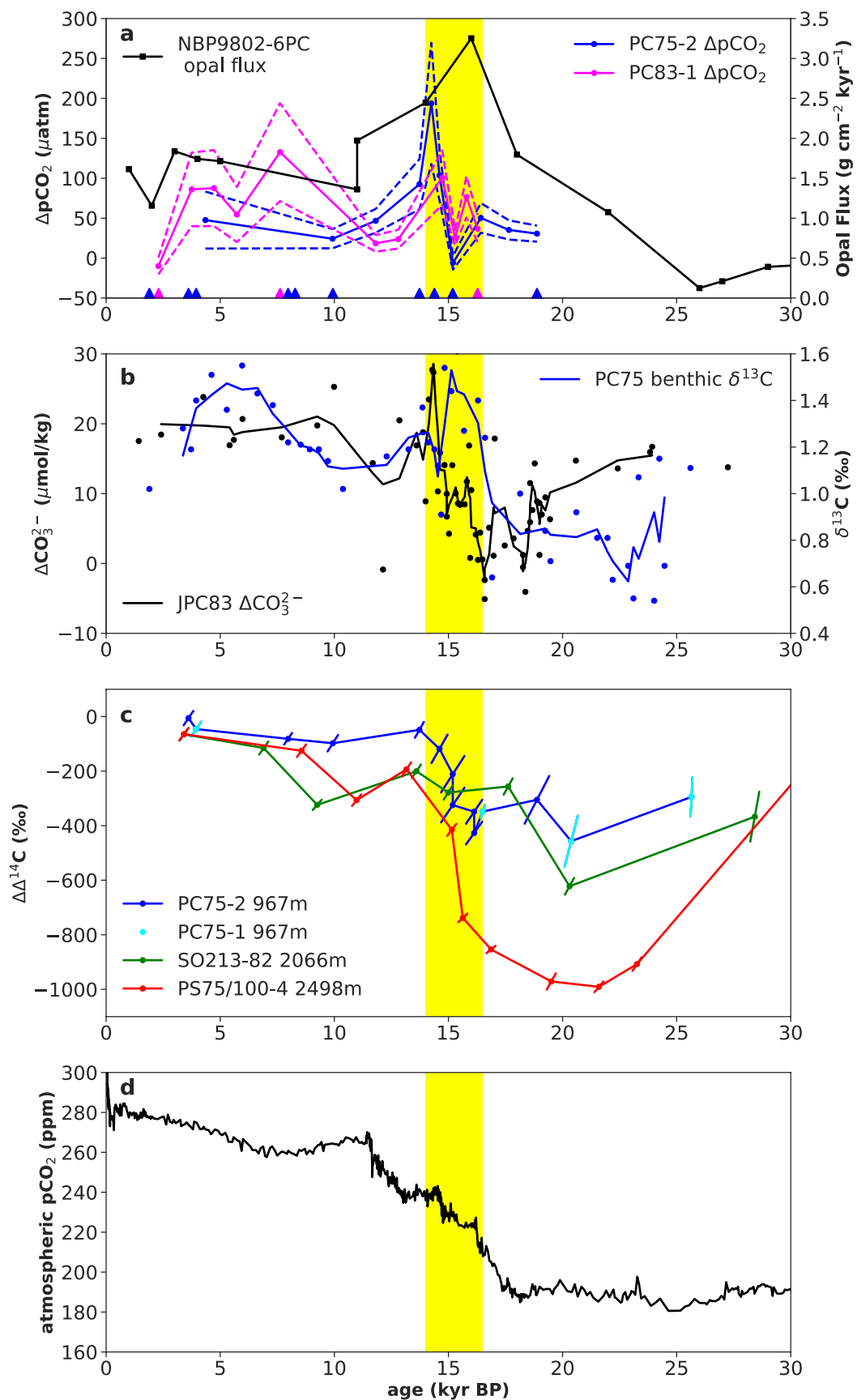




**Figure 6.** a) PC75-2 and PC83-1  $\Delta p\text{CO}_2$  plotted with an opal flux record from the SW Pacific sector of the Southern Ocean (Chase et al., 2003). The dotted envelopes represent uncertainty of  $\Delta p\text{CO}_2$  (the 14% and 86% quantile). Triangle marks represent intervals with radiocarbon age constraints as in Figure 3. b) JPC83 benthic  $\Delta[\text{CO}_3]^{2-}$  from the Bay of Plenty (Allen et al., 2015), plotted with PC75-1 (this study) benthic  $\delta^{13}\text{C}$  records. The raw data are plotted as dots; the thick lines are 3-point running averages. c) Three records of benthic - atmospheric  $\Delta^{14}\text{C}$  offset ( $\Delta\Delta^{14}\text{C}$ ) from Chatham Rise. PC75-1 and PC75-2 radiocarbon data are combined together but are labeled with different color coding. d) atmospheric  $p\text{CO}_2$  (Bereiter et al., 2015). The 16.5-14 kyrBP event is highlighted in yellow for all panels.

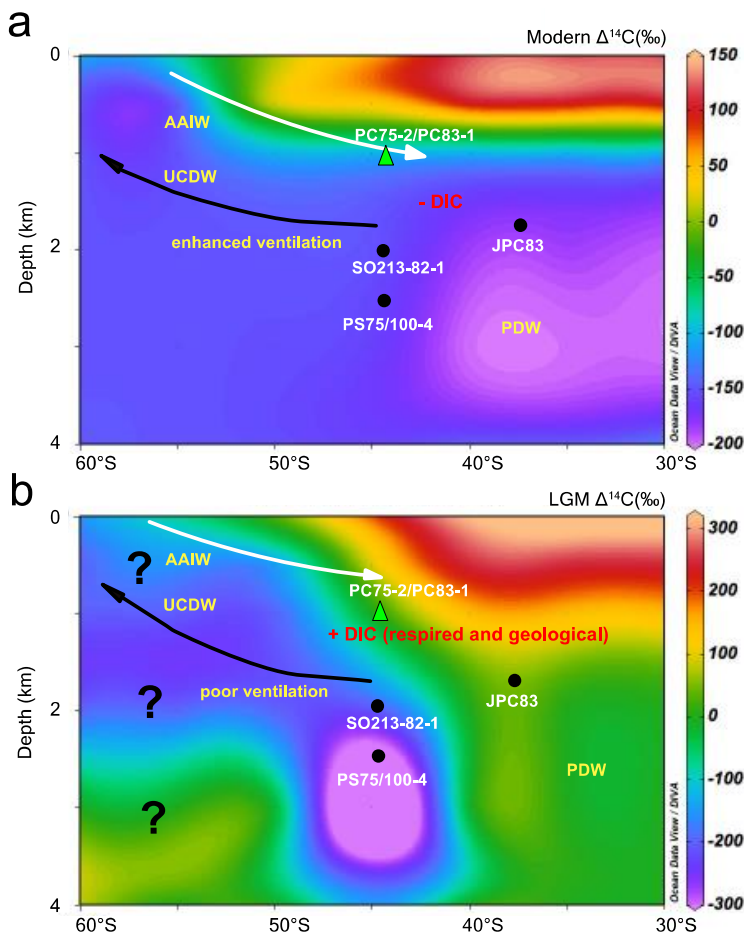


**Figure 7.** Conceptual diagrams of SW Pacific circulation and radiocarbon distribution. (a) Modern pattern. Site PC75-2 and site PC83-1 are bathed under well ventilated AAIW, with no influence of geological carbon. The color shading is based on interpolating a transect of  $\Delta^{14}\text{C}$  data between 170°E to 180°E from the GLODAP database to a 10° in latitude by 500m in depth grid. (b) LGM pattern. Site PC75-2 and site PC83-1 are bathed under poorly ventilated, respired carbon-rich UCDW. Episodic release of  $^{14}\text{C}$ -dead geological carbon makes the deep/intermediate waters as well as the surface of Southern Ocean appear to be ‘old’. The color shading is based on multiple published  $\Delta^{14}\text{C}$  records from sediment cores (not labelled in the panels) that represent glacial  $\Delta^{14}\text{C}$  signature of PDW, AAIW, SAMW in the Southern Hemisphere. The high latitude Southern Ocean is labelled with question marks due to a lack of data. Panels were generated using ODV 4.7.10.

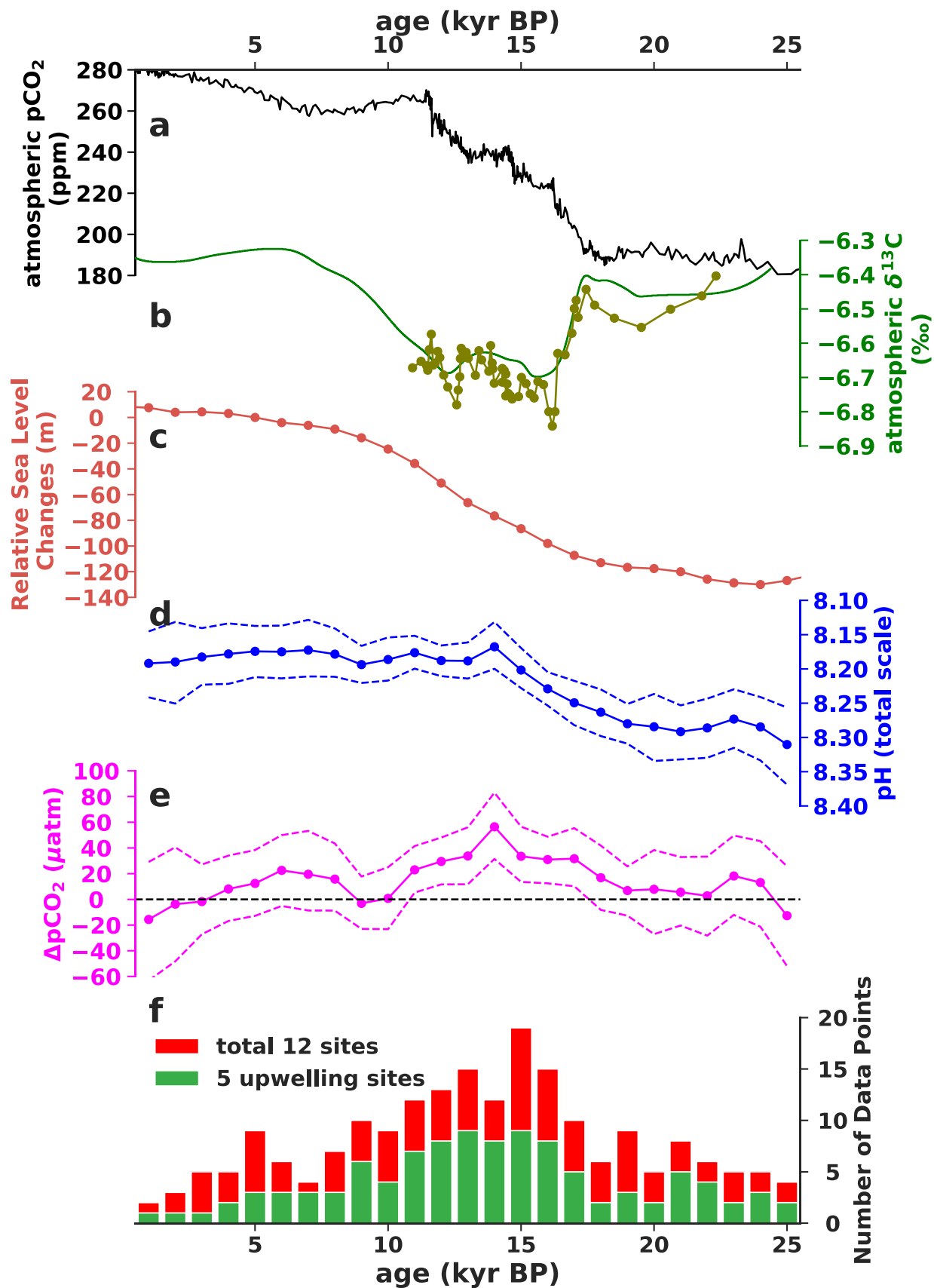


**Figure 8.** a) atmospheric pCO<sub>2</sub> (Bereiter et al., 2015); b)  $\delta^{13}\text{C}$ -CO<sub>2</sub> from Schmitt et al., 2012 (green) and Bauska et al., 2016 (Olive); c) relative sea level changes (Spratt & Lisiecki, 2016); d) the median of 10,000 composite pH from 12 cores (thick blue line), the dotted lines represent 2.5% and 97.5% quantile, the black line with triangle markers represent the median of 10,000 composite pH without our two new records; e) the median of 10,000 composite  $\Delta\text{pCO}_2$  from 12 cores (thick magenta line), the dotted lines represent 2.5% and 97.5% quantile; f) number of data points from all (red bars)/upwelling (green bars) sites that go into each 1000-yr bin. Upwelling sites include ODP1238 from the eastern equatorial Pacific, PS2498 from the sub-Antarctic Atlantic, MD01-2416 from the subarctic Pacific, NIOP464 and AAS9 from the Northern Indian Ocean.

Core name	Species	Slope ('m')	Intercept ('c')	Reference	Calibration	Technique
ODP1238	<i>T. sacculifer</i>	0.82	3.94	Martínez-Botí et al., 2015	Henehan et al., 2016	MC-ICP-MS
NIOP464	<i>T. sacculifer</i>	0.82	-0.66	Palmer et al., 2010	Henehan et al., 2016 'c' modified by this study	NTIMS
EDRC92	<i>T. sacculifer</i>	0.82	-1.66	Palmer & Pearson, 2003	Henehan et al., 2016 'c' modified by this study	NTIMS
MD01-2416	<i>N. pachyderma</i>	1	-3.38	Gray et al., 2018a	Gray et al., 2018a	MC-ICP-MS
JM11-PI-19PC	<i>N. pachyderma</i>	1	-2.053	Ezat et al., 2017	Gray et al., 2018a, 'c' modified by Ezat et al., 2017	NTIMS
ODP999	<i>G. ruber</i>	0.55	9.82	Foster, 2008	Raitzsch et al., 2018	MC-ICP-MS
GeoB1523	<i>G. ruber</i>	0.55	9.82	Henehan et al., 2013	Raitzsch et al., 2018	MC-ICP-MS
GeoB1105	<i>G. ruber</i>	0.55	9.82	Foster & Sexton, 2014	Raitzsch et al., 2018	MC-ICP-MS
AAS9	<i>G. ruber</i>	0.55	9.82	Naik et al., 2015	Raitzsch et al., 2018	MC-ICP-MS
PS2498-1	<i>G. bulloides</i>	1.09	-3.58	Martínez-Botí et al., 2015	Raitzsch et al., 2018	MC-ICP-MS
PC75-2	<i>G. bulloides</i>	1.09	-3.58	this study	Raitzsch et al., 2018	MC-ICP-MS
PC83-1	<i>G. bulloides</i>	1.09	-3.58	this study	Raitzsch et al., 2018	MC-ICP-MS

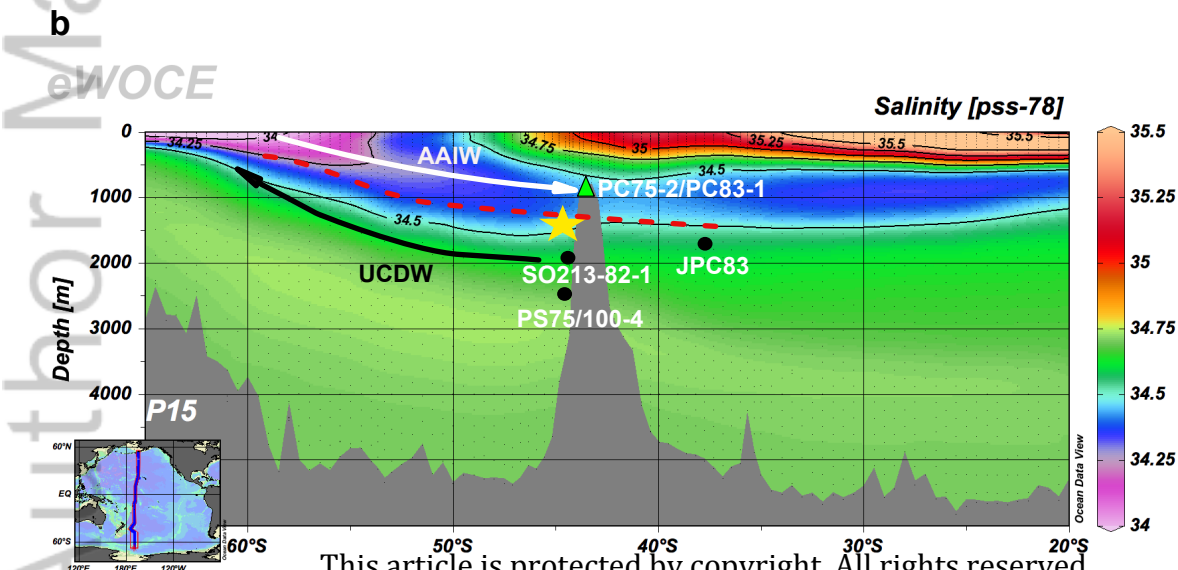
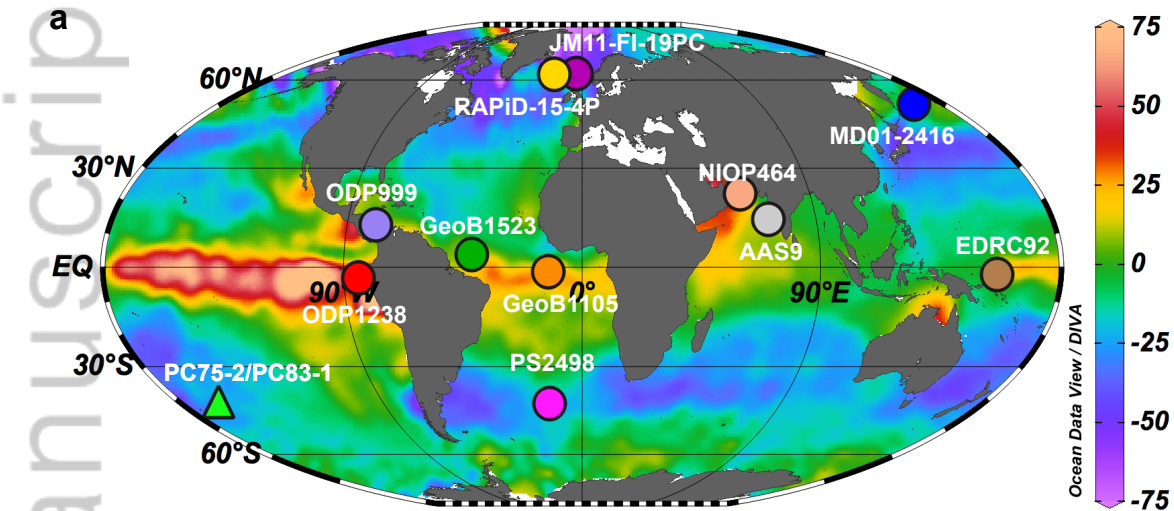
**Table 1.** Calibration curves used for each individual record; regression in the form of  $\delta^{11}\text{B}_{\text{CaCO}_3} = m^* \delta^{11}\text{B}_{\text{borate}} + c$

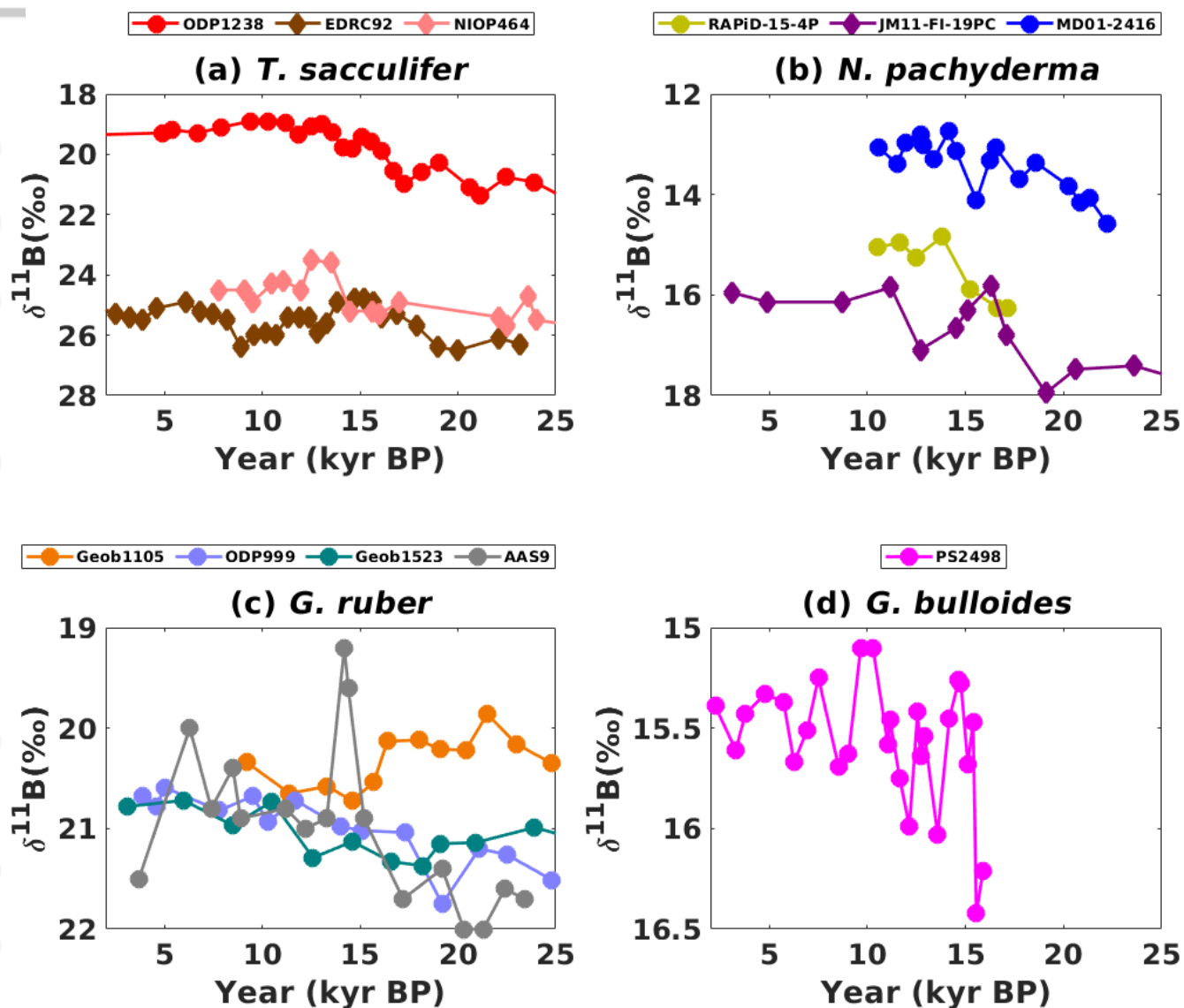
Experiment name	spin	ALK addition	CaCO <sub>3</sub> addition	DIC removal
atm pCO <sub>2</sub> (ppm)	278	184	184	181
Surface pH (total scale)	8.15	8.31	8.34	8.30
Surface ALK (μmol/kg)	2268	2350	2542	2264
Surface DIC (μmol/kg)	1953	1937	2084	1871

Table 2: Scenarios to achieve atmospheric pCO<sub>2</sub>~180ppm through surface inversion in cGENIE.

Core name	$\text{pH}_{\text{boron\_Holocene}}$ (total scale)	$\text{pH}_{\text{site\_preind}}$ (total scale)	$\text{pCO}_{2\text{boron\_Holocene}}$ ( $\mu\text{atm}$ )	$\text{pCO}_{2\text{site\_preind}}$ ( $\mu\text{atm}$ )
PC83	$8.106 \pm 0.023$	$8.214 \pm 0.119$	$339 \pm 19$	$265 \pm 77$
PC75	$8.142 \pm 0.016$	$8.214 \pm 0.119$	$304 \pm 11$	$265 \pm 77$
NIOP464	$8.095 \pm 0.015$	$8.091 \pm 0.020$	$351 \pm 15$	$355 \pm 19$
ODP1238	$8.107 \pm 0.010$	$8.081 \pm 0.027$	$335 \pm 9$	$353 \pm 26$
ODP999	$8.161 \pm 0.007$	$8.138 \pm 0.055$	$286 \pm 5$	$312 \pm 46$
GEOB1105	$8.123 \pm 0$	$8.159 \pm 0.019$	$324 \pm 0$	$294 \pm 15$
GEOB1523	$8.175 \pm 0.006$	$8.155 \pm 0.002$	$276 \pm 5$	$290 \pm 2$
AAS9	$8.245 \pm 0.013$	$8.192 \pm 0.054$	$228 \pm 9$	$262 \pm 39$
EDRC92	$8.099 \pm 0.011$	$8.091 \pm 0.033$	$332 \pm 10$	$337 \pm 29$
JM11	$8.249 \pm 0.007$	$8.240 \pm 0.002$	$233 \pm 5$	$236 \pm 1$
MD01-2416	$8.158 \pm 0$	$8.200 \pm 0.005$	$289 \pm 0$	$258 \pm 4$
PS2498	$8.154 \pm 0.007$	$8.193 \pm 0.013$	$298 \pm 5$	$267 \pm 9$

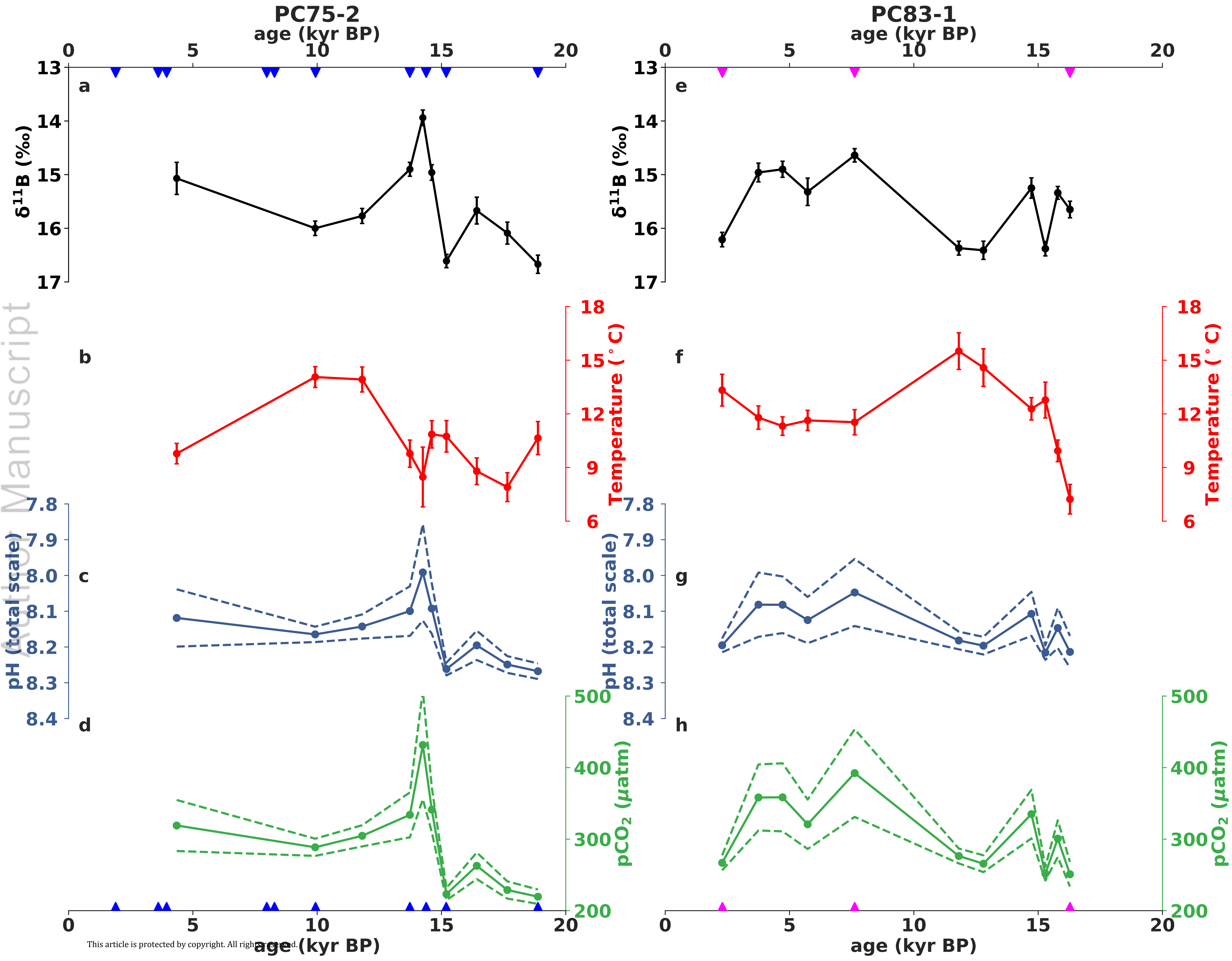
Table 3: Estimated  $\text{pH}_{\text{boron\_Holocene}}$ ,  $\text{pH}_{\text{site\_preind}}$ ,  $\text{pCO}_{2\text{boron\_Holocene}}$  and  $\text{pCO}_{2\text{site\_preind}}$  for 12 individual records with errors (1SE). Note the uncertainty for MD01-2416 and GeoB1105 record is 0 because there is only one data point in the entire Holocene period. Global mean pre-industrial sea surface  $\text{pH}=8.18$ , sea surface  $\text{pCO}_2=271\text{ppm}$ . Note the term  $\text{pH}_{\text{site\_preind}}$  and  $\text{pCO}_{2\text{site\_preind}}$  are not part of the expression to calculate  $\text{pH}_{\text{final}}$  and  $\text{pCO}_{2\text{final}}$  (see the main text) as they are canceled out when both the reconstruction bias and the location bias are taken into account.

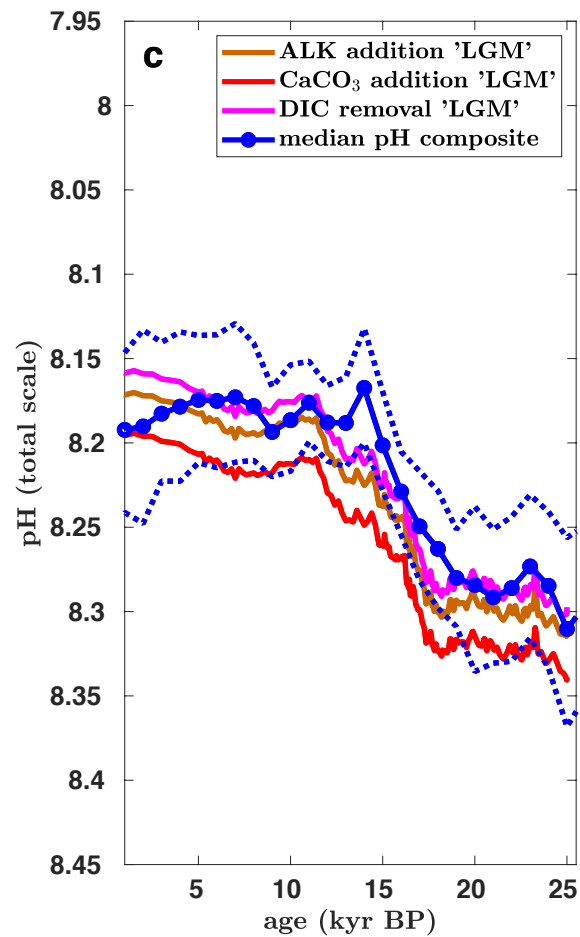
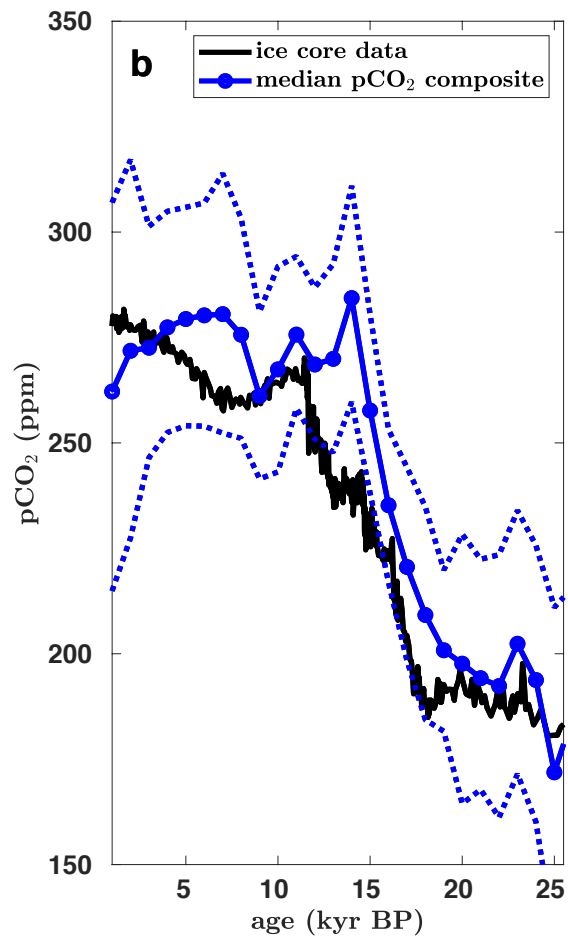
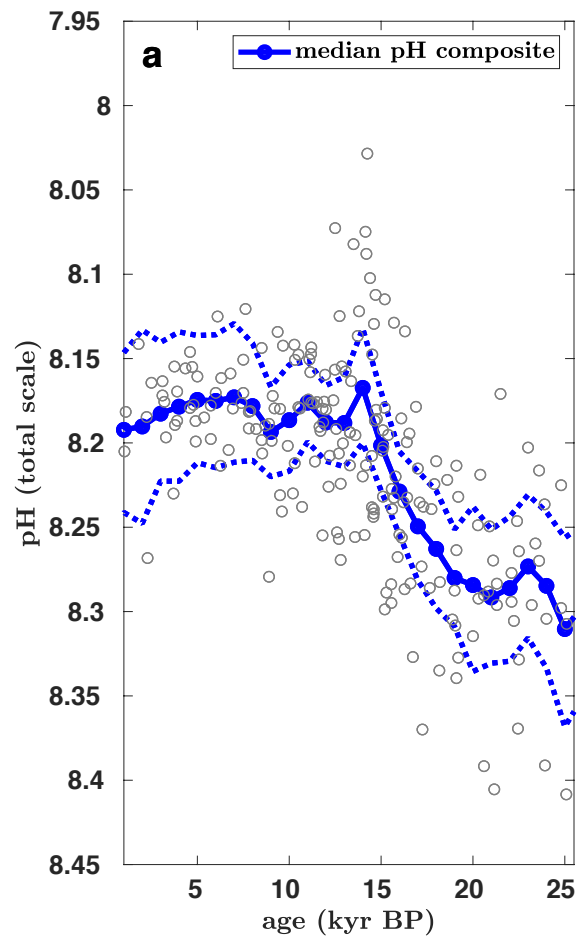


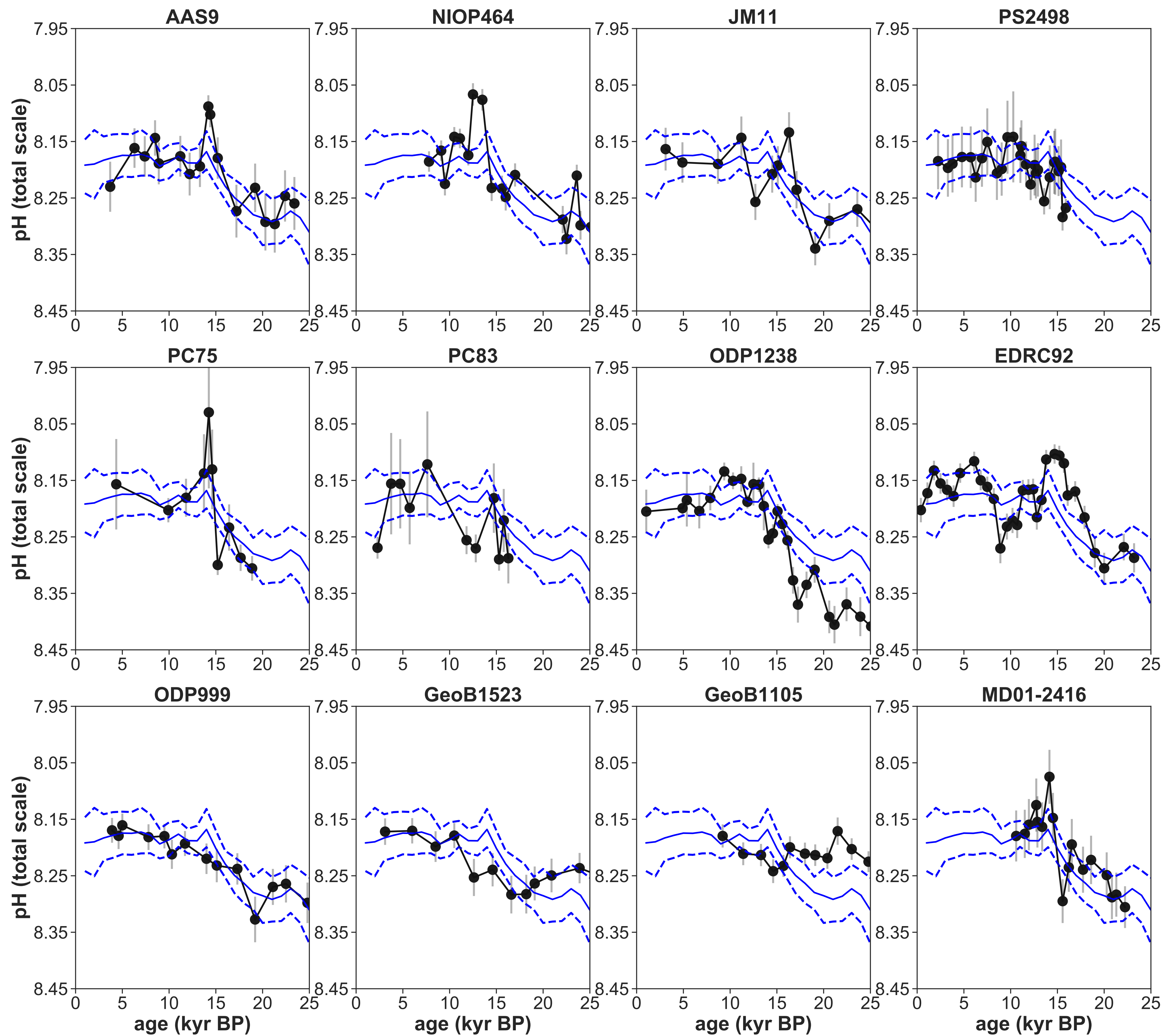


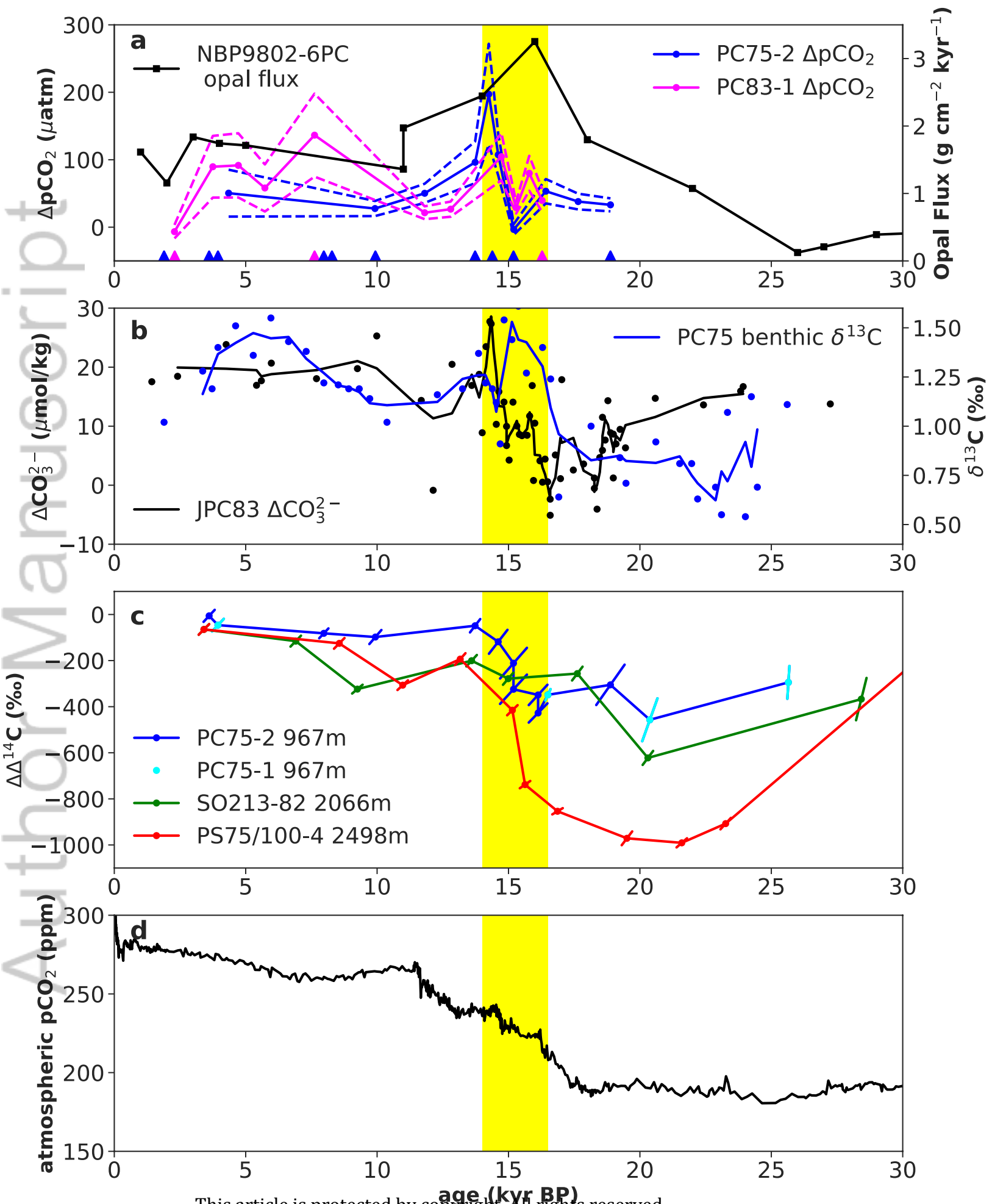
2018PA003498-f02-z.tif



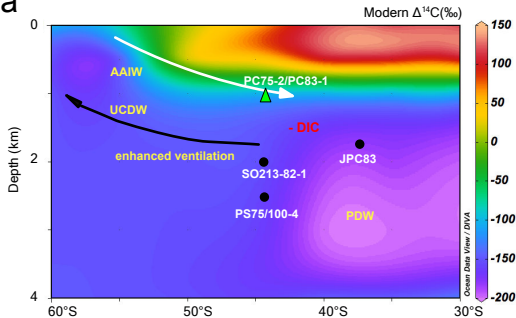




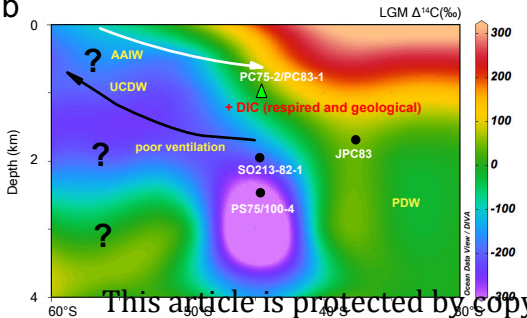




a



b



This article is protected by copyright

